UNIVERSITÉ CÔTE D'AZUR

ÉCOLE DOCTORALE
SCIENCES FONDAMENTALES ET APPLIQUÉES

UNIVERSITÀ DEGLI STUDI DI GENOVA

DOCTORAL THESIS

Acoustofluidic interferometric device

for optomechanical cytometry

Julián MEJÍA MORALES

Institut de Physique de Nice
INPHYNI

Presented for obtaining the degree of doctor in Physics **at the** Université Côte d'Azur **and** Biotechnology in Translational Medicine **at the** Università di Genova
Advisor : Gian Luca Lippi Prof. Dr. / Rodolfo Quarto Prof. Dr.
Co-Tutor : Massimo Vassalli Dr.
Defence date : 22/Feb/2021

Jury :
Huabing Yin, Prof. Dr., University of Glasgow
Tomaso Zambelli, Prof. Dr., ETH Zürich
Sylvain Gabriele, Prof. Dr., Université de Mons
Rodolfo Quarto, Prof. Dr., Università di Genova
Massimo Vassalli, Dr. University of Glasgow
Agnese Seminara, Dr., Université Côte d'Azur
Gian Luca Lippi, Prof. Dr., Université Côte d'Azur

UNIVERSITÉ FRANCO ITALIENNE | UNIVERSITÀ ITALO FRANCESE

GOBIERNO DE MÉXICO | CONACYT Consejo Nacional de Ciencia y Tecnología

Abstract

In the past years, growing demand for label-free cell analysis has emerged. This demand answers the need for cell analysis in its developing stages and, perhaps more importantly, to study physiological cell states in a simpler way than using fluorescence-based analyses. Mechanical and optical properties of cells are emerging as powerful biomarkers to discriminate cells. The cell deformation induced by acoustic pressure is measured with the Acoustofluidic Interferometric Device, developed in this thesis. It allows for studying the deformability of the cell in a way similar to what is done for the analysis of the Young modulus. Deformability is an integral biomarker that summarizes cell gene expression, and the cell refractive index is related to the density of proteins in the cytoskeleton. The Acoustofluidic Interferometric Device, developed for the measurement of optomechanical cell properties on a cytometric basis. The device is thoroughly described and characterized in this thesis. The device enables the assessment of size, deformability, and refractive index (or a combination of them) of non-adherent cells utilizing a low finesse Fabry-Perot resonator and acoustic manipulation. When an acoustically focussed cell (or another micro-sized particle) crosses the Fabry-Perot cavity axis, it will perturb the resonator's fringe pattern governed by the Airy's transmission function. Such perturbation can be characterized and analyzed by means of the parameters ρ (radii of the circular interference fringes), Full Width at Half Maximum of the individual fringe, and by the distance between fringes (Free Spectral Range). The analysis of the perturbation enables the assessment of the cell's optomechanical properties. Measurement of Algae and Yeast cells' deformability has been carried out to test the instrument's performance and compared to the equivalent perturbation introduced by Microgel beads and Polystyrene spheres as controls. The experiment is based on the cell-induced fringe pattern perturbation analysis. Images of the perturbation are acquired under two different conditions; 1) acoustic focussing and 2) acoustically induced deformation. 180 independent intensity profiles are retrieved and analyzed for each image, allowing for statistical analysis of the parameters: cell focal length and perturbed resonator Finesse. The results show a change in the optomechanical properties of the Algae, Yeast, and Microgel. Notoriously, the Polystyrene sample remains virtually unchanged, as expected since Polystyrene is much stiffer than a cell and cannot be deformed by the instrument's pressure field. These results show that the acoustofluidic technique presented here is useful to detect and measure different optomechanical properties which, potentially, can be used as label-free biomarkers in clinical diagnosis.

Keywords: Fabry-Perot interferometer, acoustic focusing, acoustic manipulation of cells, cell optomechanical properties, Fabry-Perot fringe pattern perturbation, Thin lens proxy for a cell, microfluidics, cytometry, acoustofluidic interferometric device (AID).

LABEL « DOCTORAT EUROPEEN »

Je soussigné Jeannick Brisswalter, Président de l'Université Côte d'Azur (UCA),

certifie que M. Julián Méjía Morales

né le 28/08/1990 à Azcapotzalco (Ciudad de México – anciennement Distrito Federal – Mexique)
a rempli les quatre conditions requises pour l'attribution du label « Doctorat Européen » lors de la préparation de sa thèse et de l'obtention de son diplôme de docteur d'Université de l'enseignement supérieur et de la recherche.

Sujet de la thèse : Acoustofluidic Interferometric Device for Optomechanical Cytometry

Directeur de thèse : Prof. Gian Luca LIPPI (UCA) and Prof. Rodolfo QUARTO (Università di Genova, Italy)

Rapporteurs : - Prof. Huabing YIN, University of Glasgow (UK)
- Prof. Tomaso ZAMBELLI, ETH Zürich (CH)

Jury :
- Prof. Huabing YIN, University of Glasgow (UK)
- Prof. Tomaso ZAMBELLI, ETH Zürich (CH)
- Prof. Sylvain GABRIELE, Université de Mons (BE)
- Prof. Rodolfo QUARTO, Università di Genova (I)
- Dr. Massimo VASSALLI, University of Glasgow (UK)
- Dr. Agnese SEMINARA, Université Côte d'Azur (F)
- Prof. Gian Luca LIPPI, Université Côte d'Azur (F)

Cette thèse a été soutenue en français et, partiellement, en Anglais et Italien

Le stage à l'étranger s'est déroulé du 01/05 au 31/08 2018 et du 01/06/2019 au 05/06/2020 dans l'équipe du Professeur Rodolfo Quarto de l'établissement **Università di Genova, Italie**.

- thèse en co-tutelle avec Prof. Rodolfo Quarto, Università di Genova

- thèse avec délivrance du double diplôme doctorat français en **Physique**/ doctorat italien en **Biotechnology in Translational Medicine**

DOCTOR EUROPEUS

Fait à Nice, le - 8 MARS 2021

Signature du Président
et cachet de l'établissement

Pour le Président et par délégation
Pascale STEICHEN
Vice-Présidente politique doctorale et post-doctorale

Dedication

To my beloved family and friends

Acknowledgements

For their direct contribution to the successful conclusion of this work:
Prof. Dr. Gian Luca Lippi, Dr. Massimo Vassalli, Prof. Dr. Rodolfo Quarto, Prof. Dr. Peter Glynne-Jones, Dr. Marco Satore, Dr. Stéphane Barland, Dr. Chiara Gambardella, Dr. Elisabeth Taffin de Givenchy, Dr. Salvatore Girardo, Prof. Dr. Jochen Guck, INPHYNI-CNRS-UCA staff, IBF-CNR-UNIGE staff.

For their unconditional support:
My family, my friends

For all that they have taught me:
Prof. Dr. Gian Luca Lippi, Dr. Massimo Vassalli

For making this journey enjoyable:
My friends, my family, INPHYNI-CNRS-UCA people, IBF-CNR-UNIGE people

For funding this project:
Consejo Nacional de Ciencia y Tecnología de México (CONACyT), Scholarship 471712.
Université Franco-Italienne, VINCI funding C2-1031

INDEX

List of Tables

Table **Page**

List of Figures

Figure **Page**

CHAPTER 1

INTRODUCTION

This thesis has an interdisciplinary character, exploiting advanced physical methods to study single living cells' physiology with high throughput. For this reason, it is essential to review the physics used to retrieve information and the cells' physiologic properties, which are the object of study. Light interference is used to analyze cells' optical properties in a novel way, and in combination with acoustics, is used to assess cell deformability, a useful parameter for cell characterization. In the following pages, we will see how and why.

All together, light interference, cell mechanical properties, and acoustic cell manipulation are central for this work. The combination of optics acoustics and cytometry enabled us to innovate in single-cell characterization. This introduction is intended to justify this combination, provide the theoretical background, and identify the technology's scope and limitations. In the first section, a detailed review of the Fabry-Perot theory and its applications in biology are presented, followed by a revision of the cells' mechanical properties, and finally, the main techniques for mechanical properties assessment.

1.1 Interferometry

1.1.1 Fabry-Perot interferometer

An optical resonator is an arrangement of mirrors that allows light to circulate in a closed path. The simplest kind of optical resonator consists of two reflecting mirrors facing each other at a distance L, and it is also known as Fabry-Perot cavity. It is possible to compute the complex amplitude of the electromagnetic wave resonating inside the cavity E_{cav} and the transmitted E_{tr} and reflected E_{ref} amplitudes of the electromagnetic waves.

The convention used to indicate the phase shift of π that experiences the reflected field when travelling from the medium with the lower refraction index to the medium with the higher refraction index will be $E_{\text{ref}} = -r \cdot E_{\text{in}}$. Every time that a wave makes a partial trip inside the cavity it acquires a phase shift of $nkL\cos\theta$, or for a round trip:

$$\delta = 2nkL\cos\theta, \tag{1.1}$$

let be n the media refractive index in between the mirrors, k is the vacuum wavenumber and θ the angle of incidence of the light onto the mirrors.

For a cavity with two mirrors (M_1 , M_2) with reflection coefficients r_1 , r_2 (ratio of reflected and incident amplitudes), transmission coefficients t_1, t_2 (ratio of transmitted and incident amplitudes) separated by a distance L (see Fig. (1.1)), the electromagnetic field at different points can be written as:

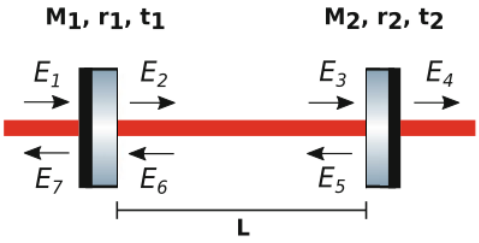

FIGURE 1.1. Schematics of a Fabry-Perot cavity. Notice that the reflective part of the mirror, its coating, is placed in the inner part.

$$\begin{aligned} E_2 &= t_1 \cdot E_1 - r_1 \cdot E_6 & \qquad E_5 &= -r_2 \cdot E_3 \\ E_3 &= E_2 \cdot e^{i\delta/2} & \qquad E_6 &= E_5 \cdot e^{i\delta/2} \\ E_4 &= t_2 \cdot E_3 & \qquad E_7 &= r_1 \cdot E_1 + t_1 \cdot E_6 \end{aligned} \tag{1.2}$$

where E_1 is the input field.

The reflected field E_7 , has two contributions: one coming from the directly reflected beam and the second one coming from the field inside the cavity being transmitted through the input mirror. This intra-cavity field is the result of the interference between the partial waves that are circulating inside the cavity.

From the expressions above the following equations can be derived:

- Intra-cavity field (E_2):

$$\begin{aligned} E_2 &= t_1 \cdot E_1 - r_1 \cdot E_6 \\ E_{\text{cav}} = E_2 &= t_1 \cdot E_1 - r_1 \cdot \left[-r_2 \cdot \left(E_2 \cdot e^{i\cdot\delta/2} \right) \cdot e^{i\cdot\delta/2} \right] \end{aligned}$$

$$E_{\text{cav}} = E_1 \cdot \frac{t_1}{1 - r_1 \cdot r_2 \cdot e^{i\cdot\delta}} \tag{1.3}$$

- Reflected field (E_7):

$$\begin{aligned} E_7 &= r_1 \cdot E_1 + t_1 \cdot E_6 \\ E_7 &= r_1 \cdot E_1 + t_1 \cdot \left(-r_2 \cdot E_2 \cdot e^{i \cdot \delta} \right) \\ E_{\text{ref}} = E_7 &= r_1 \cdot E_1 + t_1 \cdot \left(-r_2 \cdot E_1 \cdot \frac{t_1}{1 - r_1 \cdot r_2 \cdot e^{i \cdot \delta}} \cdot e^{i \cdot \delta} \right) \end{aligned}$$

$$E_{\text{ref}} = E_1 \cdot \left[\frac{r_1 - r_2 \cdot \left(r_1^2 + t_1^2 \right) \cdot e^{i \cdot \delta}}{1 - r_1 \cdot r_2 \cdot e^{i \cdot \delta}} \right] \tag{1.4}$$

- Transmitted field (E_4):

$$\begin{aligned} E_4 &= t_2 \cdot E_3 \\ E_4 &= t_2 \cdot E_2 \cdot e^{i \cdot \delta/2} \\ E_{\text{tr}} = E_4 &= t_2 \cdot E_1 \cdot \frac{t_1}{1 - r_1 \cdot r_2 \cdot e^{i \cdot \delta}} \cdot e^{i \cdot \delta/2} \end{aligned}$$

$$E_{\text{tr}} = E_1 \cdot \frac{t_1 \cdot t_2 \cdot e^{i\delta/2}}{1 - r_1 \cdot r_2 \cdot e^{i \cdot \delta}} \tag{1.5}$$

However, these expressions are the complex amplitudes of the respective fields while in practice the measurable quantity is the power. So, starting from eq. (1.5) the power transmitted by a Fabry-Perot cavity can be written as:

$$P_{\text{tr}} \propto E_{tr} \cdot E_{tr}^* = P_{\text{in}} \cdot \frac{t_1^2 \cdot t_2^2}{1 + r_1^2 \cdot r_2^2 - 2 \cdot r_1 \cdot r_2 \cdot \cos(\delta)}. \tag{1.6}$$

Irradiance is proportional to the square of the magnitude of the field amplitude, $P_{\text{tr}} \propto E_{\text{tr}} \cdot E_{\text{tr}}^*$, so the transmittance T of the Fabry-Perot cavity is:

$$T \equiv \frac{P_{\text{tr}}}{P_{\text{in}}} = \frac{t^4}{1 + r^4 - 2 \cdot r^2 \cdot \cos(\delta)}, \tag{1.7}$$

where the mirrors has being considered to being with the same properties t_1, $t_2 = t$ and r_1, $r_2 = r$. Using the trigonometric identity $\cos\delta = 1 - 2\sin^2(\delta/2)$, the lossless mirror condition $t^2 = 1 - r^2$ [79] and simplifying a bit allows the transmittance to be put into the form of the Airy function,

$$T = \frac{(1 - r^2)^2}{1 - 2 \cdot r^2 + r^4 + 4 \cdot r^2 \cdot \sin^2(\delta/2)},$$

$$T = \frac{1}{1 + \left[\frac{4 \cdot r^2}{(1 - r^2)^2} \right] \cdot \sin^2(\delta/2)}. \tag{1.8}$$

Analogously, for the reflected irradiance R, $P_{\text{ref}} \propto E_{\text{ref}} \cdot E_{\text{ref}}^*$, from eq. (1.4):

$$R \equiv \frac{P_{\text{ref}}}{P_{\text{in}}} = \frac{r_1 - r_2 \cdot \left(r_1^2 + t_1^2\right) \cdot e^{i \cdot \delta}}{1 - r_1 \cdot r_2 \cdot e^{i \cdot \delta}} \cdot \frac{r_1 - r_2 \cdot \left(r_1^2 + t_1^2\right) \cdot e^{-i \cdot \delta}}{1 - r_1 \cdot r_2 \cdot e^{-i \cdot \delta}} \tag{1.9}$$

$$R = \frac{2 \cdot r^2 (1 - \cos\delta)}{1 + r^4 - 2 \cdot r^2 \cdot \cos\delta}$$

$$R = \frac{4 \cdot r^2 \cdot \sin^2(\delta/2)}{(1 - r^2)^2 + 4 \cdot r^2 \cdot \sin^2(\delta/2)}$$

$$R = \frac{1}{1 + \left[\frac{4 \cdot r^2}{(1 - r^2)^2}\right] \cdot \csc^2(\delta/2)}. \tag{1.10}$$

1.1.1.1 Coefficient of finesse

Fabry called the square-bracketed factor in eq. (1.8) – an exclusively function of the mirrors' reflection coefficient r– the coefficient of finesse, F:

$$F = \frac{4 \cdot r^2}{\left(1 - r^2\right)^2}, \tag{1.11}$$

Or in terms of the reflectance [10],

$$r \cdot r^* = r^2 = \mathrm{R}, \tag{1.12}$$

the coefficient of Finesse takes the form

$$F = \frac{4 \cdot \mathrm{R}}{(1 - \mathrm{R})^2}. \tag{1.13}$$

This definition allows for a more compact for the Airy's transmission function eq. (1.8):

$$T = \frac{1}{1 + F \cdot \sin^2(\delta/2).} \tag{1.14}$$

And for reflectance:

$$R = \frac{1}{1 + F \cdot \csc^2(\delta/2).} \tag{1.15}$$

1.1.1.2 Resonance condition

The resonance condition occurs when the phase shift δ eq. (1.1) corresponds ton an integer multiple m of 2π the interference is constructive and the cavity is on resonance

$$\delta = 2 \cdot n \cdot k \cdot L \cdot \cos\theta = m \cdot 2 \cdot \pi \tag{1.16}$$

Figure (1.2) shows that this phase shift leads to a maximum on the transmittance. When substituting in Eqs. (1.3) and (1.4) it can be seen that it also corresponds to a minimum of the reflected power [13, 79].

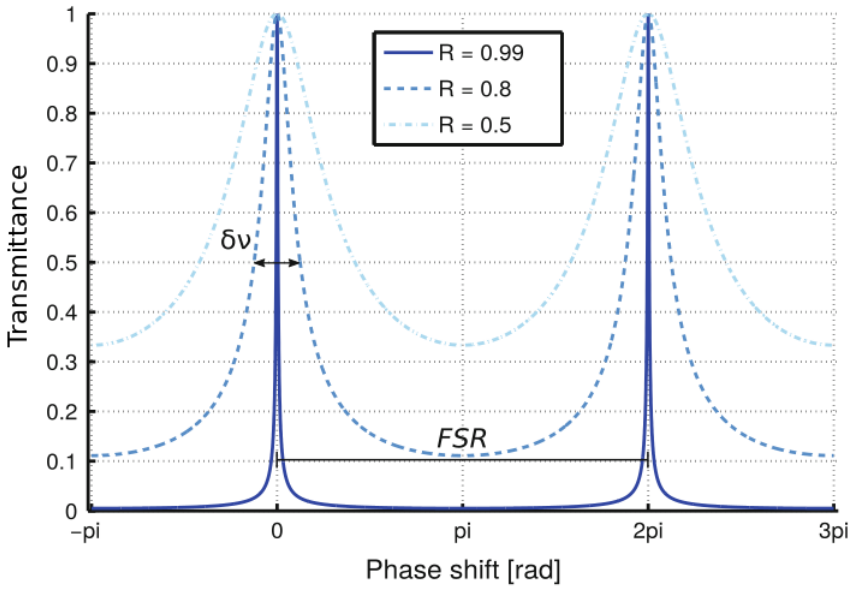

FIGURE 1.2. Fabry-Perot cavity transmitivity as a function of the phase shift accumulated in a round-trip shows an Airy function. In the figure three different mirrors reflectivities R = $r \cdot r*$ are shown: R = 0.99, R = 0.8, R = 0.5. No losses were considered ($t + r = 1$). δ_ν is the cavity linewidth and FSR the free spectral range. Modified from [13].

1.1.1.3 Free Spectral Range (FSR)

The Free Spectral Range (FSR) is the frequency difference between two consecutive resonances. From resonance condition eq. (1.16) and the dispersion relation can be derived the following condition for the FSR,

$$\mathrm{FSR} = \Delta\nu = \frac{c}{2 \cdot n \cdot L \cdot \cos\theta} \tag{1.17}$$

Also from the resonance condition is clear that the phase difference between two adjacent resonances is:

$$\delta_{\mathrm{FSR}} = 2\pi \tag{1.18}$$

1.1.1.4 Finesse

The Coefficient of Finesse F is not to be confused with a second commonly used figure of merit $\mathscr{F}$, called simply the Finesse. The Finesse $\mathscr{F}$ is the ratio of the FSR to the Full-Width at Half-Maximum (FWHM) of the peaks (also called linewidth).

$$\mathscr{F} = \frac{\pi}{2 \cdot \arcsin\left(\frac{1}{\sqrt{F}}\right)} \approx \frac{\pi\sqrt{F}}{2} = \frac{\pi \cdot \sqrt{r}}{1 - r} \tag{1.19}$$

1.1.1.5 FWHM

The half-width at half-maximum (HWHM) $\delta_{1/2}$ of the transmittance peaks (see fig (1.2)) can be found from eq. (1.14) by showing that when $T = 1/2$,

$$\sin^2(k \cdot L) = \sin^2(\delta/2) = \frac{\pi^2}{4 \cdot \mathscr{F}} \tag{1.20}$$

Equation 1.20 is valid only for for high reflectance mirrors $R > 0.5$. Trigonometric identities and a small angle approximation can be used to verify that, at the half-maximum,

$$\sin^2(\delta/2) = \sin^2(m \cdot \pi + \delta_{1/2}/2) = \sin^2\left(\frac{\delta_{1/2}}{2}\right) \approx \left(\frac{\delta_{1/2}}{2}\right)^2 \tag{1.21}$$

Combining the previous expressions, is obtained again the Finesse as ratio between the Free Spectral Range and Full With at Half Maximum:

$$\delta_{1/2} = \pi/\mathscr{F}. \tag{1.22}$$

Cavities with more highly reflecting mirrors have higher values for the Finesse and so narrower transmittance peaks than those cavities with less highly reflecting mirrors [79]. As said, the Finesse of a cavity is the ratio of the free spectral range of the cavity to the FWHM of the cavity transmittance peaks:

$$\frac{\text{FSR}}{\text{FWHM}} = \frac{\delta_{\text{FSR}}}{2 \cdot \delta_{1/2}} = \mathscr{F} \tag{1.23}$$

1.1.1.6 Storage time

Storage time is the mean photon storage time inside a FP cavity before it escapes through one of the mirrors [13]. It can be calculated from the relationship between the linewidth (FWHM) of the spectrum of an exponentially decreasing electromagnetic wave and the decay time:

$$\tau = \frac{1}{2 \cdot \pi \cdot \delta_{1/2}} = \mathscr{F} \cdot \frac{2 \cdot L}{c \cdot \pi} \tag{1.24}$$

1.1.1.7 FP two beam interferometer

A Fabry-Perot interferoemter is a multiple-beam interferometer while Michelson interferometer or March Zender interferometer are two beams interferometers [10]. Nevertheles, for low reflectivity (less than 4%) the FP can be considered as a two-beam interferometer [27].

Thus, its reflected light intensity can be expressed as:

$$I = I_1 + I_2 + 2\sqrt{I_1 I_2}\cos\phi \tag{1.25}$$

where I_1 and I_2 are the intensities of the two beams reflected from the two cavity interfaces and $\phi = 4\pi nL/\lambda + \phi_0$; n is the refractive index of the medium in the FP Cavity, L is the cavity length, λ is the vacuum wavelength of the light source, and ϕ is its initial phase.

1.1.2 Interferometric microscopy

Interferometric Microscopy (IM) provides complex field information for a variety of samples at the diffraction limit. The label-free nature of these technique makes it particularly suitable for studying biological samples in a minimally invasive way for an extended period of time. IM enables measurement of the quantitative phase over the field of view with high resolution in space and time. The measured phase represents the cumulative effect of the morphology and the Refractive Index (RI) distribution of the specimen in distorting the transmitted wavefront. This phase delay, in the case of eukaryotic cells, has been shown to be linked to the cellular dry mass, which provides a powerful tool for studying cellular processes such as cell division and growth over days or weeks. When either of RI or morphology of the sample is known, one can measure the other without ambiguity [46].

In the case of red blood cells RBCs in healthy individuals, where cellular RI can be approximated with good precision, IM provides an accurate measurement of the morphology with nanometer precision [46], hence the change in the cells' morphology indicates the progression of a disease.

IM can provide complex field information of the biological samples with a high spatial and temporal resolution with virtually no photodamage by using light sources in mW order. Measuring wavelength-dependent information, in particular, has a wide range of applications, from cell and tissue refractometry to cellular biophysical measurements. IM measurements at multiple wavelengths are typically associated with a loss in temporal resolution, field of view, stability, sensitivity and may involve using expensive equipment such as tunable filters or spatial light modulators [46].

1.1.3 Interferometric biological applications

It is possible determine particle size, number density, and velocity utilizing a laser interferometer by analyzing the generated fringe pattern [31]. When the fringe spacing is comparable to a particle diameter, size can be estimated. When the fringe spacing is much greater than the average particle diameter, number density can be measured.

Mie scattering, commonly employed to determine size and spatial distribution of spherical micro-sized particles, has been adapted to collect on a defocussed image plane the reflected and first-order refracted light scattered by an aerosol [81, 115].

If the scattering particle of Fig. (1.3) is observed in the focal plane of an optical system, two "glare points" associated with the reflected and refracted rays are observed. If a sensor is now placed outside the focal plane, interference fringes appear. Placing a sensor away from a focal plane, interference fringes originating from the two imaged sources now appear [66].

This experiment is performed with standard 45 μm polystyrene particles exploiting that particle diameter is related to the interferogram's fringe spacing the particle size is determined with $\sim 1\%$ error [81]. Additionally, this method can simultaneously detect center location with high accuracy, which, coupled to tracking velocimetry techniques, can also provide information about the velocity.

Similarly, crossed-beam interferometry can be used to obtaining real-time in situ size and velocity of spherical particles or droplets [5]. The optical arrangement, consists of two laser beams focused to a crossover region. Droplets passing through the focal volume scatter light to the collecting lens situated

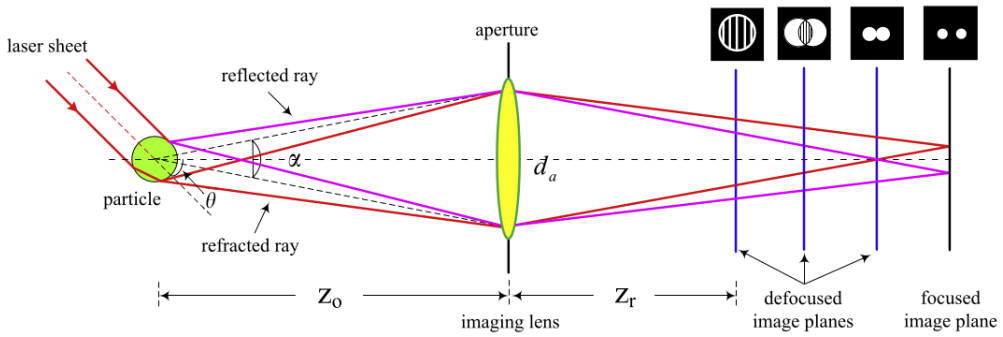

FIGURE 1.3. Schematic of interferometric imaging of particle scattering light. Taken from [81].

at some off-axis angle. The scattered light is analyzed through geometrical optics to connect the fringe pattern to the droplet diameter. Picturing the small droplets as small spherical lenses (as in Fig. (1.3)), the standing wave pattern generated by the two laser beams is magnified according to the lens's effective curvature (thus, diameter). The far-field observation of the imaged fringe pattern enables the removal of the near-field contributions present close to the scatterers. The technique can be applied to spray-droplet measurements over the size range of 3 μm to 5 mm.

In a different scheme, integration of light illumination and of optical tweezers in an inverted microscope allows for an interference-based method for measuring the cellular response to deformation [69]. The fringes, generated by transmitted and reflected light and recordered by a CMOS camera, allow for a reconstructing of cell height and morphology (as tested on fluorescence-stained HeLa cells – Cervical Epithelial Cell Line). After image processing and fringe center detection, the height of cell was estimated to be 1.16 μm. Also differences of refractive index were reported negligible for different cell parts, and ranged from 0.0339 to 0.0299 between cells and medium, in general the low RI contrast is challenge to overcome when analyzing cells by interferometric means.

A microcavity in-line Mach-Zehnder interferometer generated in an optical fiber and treated chemically for optical detection specificity, is a biosensor that can be used to monitor real-time biological phenomena. The developed biosensor exhibits ultrahigh refractive index sensitivity of 15,000 nm/RIU and is capable of detecting live E. coli bacteria concentrations as low as 100 colony forming units (CFU)/mL in liquid volume as low as picoliters [56]. This kind of biosensor can be used also for immunoglobulin G monitoring [109].

By placing transfected mammalian cells HEK293 with a plasmid encoding for expressing GFP inside a high-Q microcavity FP resonator formed by two highly reflective distributed Bragg reflectors, separated by d = 20 μm, a bio-laser (a laser with biological active media) is created. On optical pumping with nanojoule/nanosecond pulses, individual cells produce bright, directional and narrowband laser emission, with characteristic longitudinal and transverse modes Fig. (1.4). Remarkably, lasing cells remained alive even after prolonged lasing action [34].

In a similar configuration but not for single-cell analysis rather tissue analysis, a laser-based emission detection technology for biological samples is currently being developed by microfabricating an spacer with a fixed height on the top mirror of the Fabry-Perot (FP) cavity, which produces reproducible and

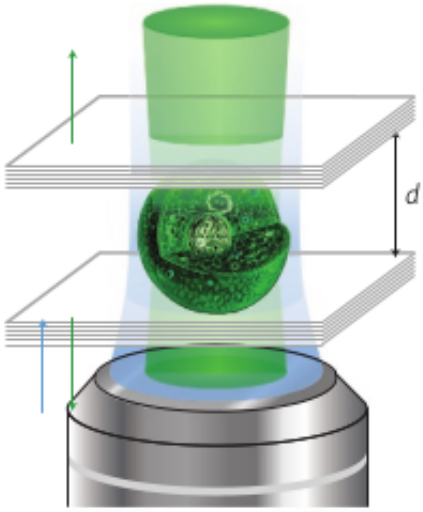

FIGURE 1.4. Illustration of the single-cell laser. A live eGFP-expressing HEK293 cell is placed inside a high-Q resonator consisting of two DBRs (d = 20 μm). Taken from [34].

stable lasing results regardless of tissue thickness. This platform has also been shown to achieve lasing emission from formalin-fixed, paraffin-embedded (FFPE) lung tissues and that cancer and normal FFPE lung tissues can be distinguished by their respective lasing thresholds [15].

1.1.4 Interferometric microfluidic applications

It is also possible to use a Fabry-Perot cavity for microfluidic velocity measurement. The reflection interference fringes are observed to fluctuation by changing; microfluidic velocity, thickness of the polyethylene film or concentration of the measured microfluidic .The cavity is formed by a Single Mode Fiber (SMF), a Bare Fiber Adapter (BFA) with polyethylene film covered on the end face. Through monitoring the interference fringe intensity or the wavelength shift, the highest microfluidic velocity sensitivity of 0.0059 nm/(μL/min) has been reached [48].

1.2 Mechanical properties of single-cells

After reviewing the interferometry theory and its successful cytology applications, we are ready to review the cells' mechanical properties and how they are related to cells' physiological states. It is essential to have a detailed description of how the physiological state changes are related to the cell's actual condition, named develop state or health state. The applications based on physical cell properties, both existing and potential, are presented and discussed later in section 4.3.

Living organisms experience different conditions like growing, aging, sickness, and death, these conditions are also shared by their basic unit: the cell. Such cell changes are physicochemical. These changes often carry change in the shape, stiffness, and deformability of the cell, referred to all together as mechanical properties of the cell. Besides, these changes can lead to a change in the cell RI. We will refer to all these properties (and their changes) as the cell's physiological state.

Understanding the mechanical properties of single cells is integral to understanding general cell and tissue behavior, becoming increasingly crucial for biophysical prevention, diagnosis, and therapies (translational applications). The mechanical properties of cells (or mechanical biomarkers) describe the deformability, or the resistance to deformation, of a cell in response to an applied load. Deformability (or effective stiffness) is akin to other characteristic properties, such as gene and protein expression, used to phenotype cell populations. Still, deformability differs in that it is an integrative characteristic of many molecular changes [21, 57]. Molecular analysis is intended for specificity, while mechanics is expected to be a more general feature. Hence it is more suitable for early screening than identification but can also contribute to diagnosis and prognosis.

The mechanical properties of single cells are just one side of the coin. Since cells are not only susceptible to mechanical changes, cells can detect and respond to mechanical stimuli often coming from surrounding cells in a process known as mechanosensitivity. Cells in vivo are continuously subjected to mechanical forces, including shear, compressive, and extensional forces. Cells' ability to deform and actively respond to mechanical forces is critical, for instance, in embryonic development or homeostasis, in adult tissues and organs [111]. The way a cell senses and response to a physical force can vary based on the cell type or tissue microenvironment, potentially altering downstream events such as migration, homeostasis, differentiation, proliferation, or tumorigenesis [24].

An essential physiological process that is an excellent example of the relevance of mechanical properties is mitosis. At anaphase, the average elasticity of cells was higher than that at other phases. Cholesterol depletion with MβCD led to an increase in the average elasticity, whereas the average roughness of the membrane surface decreased in the absence of cholesterol. As shown in Fig. (1.5), MCF-7 cells had average elasticity modulus of (18 ± 5), (19 ± 4), (31 ± 13), and (18.65 ± 7.85) – all in units kPa – at interphase, metaphase, anaphase, and telophase, respectively. At anaphase, the cell elasticity was significantly different from those at the other three phases ($P < 0.05$) [58].

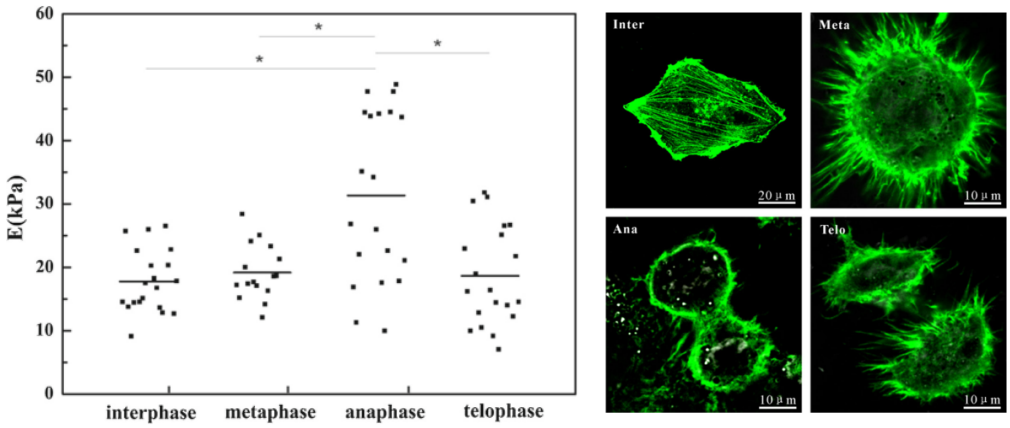

(a) Elastic distribution of cells during mitosis

(b) Confocal images during mitosis

FIGURE 1.5. (a) The elastic distribution of MCF-7 cells during mitosis (*P < 0.05). (b) The confocal images of microfilaments distribution of MCF-7 cells during mitosis. Adapted from [58].

During mitosis, the cytoskeleton is responsible for chromosome movement. It reorganizes cell structure, preparing it for division, showing that this intricate network of protein filaments makes up a dynamic, continuously reorganizing framework rather than a static scaffolding.

1.2.1 Cytoskeleton

As its name suggests, the cytoskeleton is the element that provides rigidity and structure to cells as the skeleton does for vertebrates, hence is the most relevant participant when talking about cells mechanical properties. The cytoskeleton has a central participation sustaining a cell shape, cell locomotion, and the various organelles' movement within the cell itself. The main components of the cytoskeleton are microfilaments, intermediate filaments, and microtubules.

Microfilaments are linear polymers of actin subunits that can assemble into helical filaments (F-actin). They resist tension in the cell and can polymerize or depolymerize within minutes, facilitating efficient cell motility. Microfilaments also maintain the positioning of organelles in the cell and provide overall resistance to deformation from external stimuli.

Intermediate filaments serve primarily to provide structure in cells and have been classified as vimentins, keratin, neurofilaments, lamin, and desmin. They form an elaborate network in the cytoplasm, extending from the nucleus, whose lamina mostly comprises intermediate filaments (lamins), to the plasma membrane. Intermediate filaments connect with other cytoskeletal elements, organelles, and the cell membrane to form a fully connected network.

Microtubules are polymers of tubulin that serve as a structure to transport intracellular components throughout the cell during normal biological processes while also contributing to overall cellular structure and behavior. Microtubules resist compression, as opposed to microfilaments and intermediate filaments.

In addition to the three main cytoskeletal elements, many other proteins are critical to the mechanical network's overall functionality. Of particular interest are nucleocytoskeletal proteins that link the nucleus to the cytoskeleton [55].

1.2.2 Cell membrane

The cell membrane is an integral contributor to cellular mechanical behavior due to its numerous connections to the underlying cytoskeleton. It effectively distributes external forces acting on the cell to the intracellular tensile and compressive elements as a viscoelastic covering. Alone, the cell membrane has relatively weak mechanical properties, as demonstrated by its high local extensibility when tethers are pulled away from its surface [21, 100].

1.2.3 Nucleus and other organelles

Although the nucleus and organelles are thought to serve primarily biochemical functions, their presence can also influence both local and whole-cell mechanical property measurements. The relative contributions of organelles depend, in large part, on the physical size of each component. The morphology of a cell can also influence how much the nucleus contributes to its mechanical properties. High-resolution elasticity maps of spread or flattened cells show significantly different mechanical properties for measurements made over the nucleus versus over cytoplasmic and cytoskeletal areas [14, 20]. The nucleus has been hypothesized to serve as the ultimate mechanosensory unit in the cell, where propagated forces or strains, or both. Such changes alter gene transcription. This potential role has spurred an extensive investigation into whole-cell mechanical properties and nuclear mechanical properties as a means for characterizing cell type.

1.2.4 Somatic cells

A structure-function relationship exists at the cell level, which necessitates that mechanical properties be well suited to the microenvironment provided by the surrounding tissue. Empirical evidence suggests that this cell-tissue accommodation can result in mechanical characteristics that can be used to identify cell types, and even subpopulations of cell types, in specific tissues [21, 22, 99].

Somatic cells span an extensive range of elastic properties, from very soft neuronal cell types to much stiffer bone and muscle cell types. Compliant, or soft, cell types, such as neurons and myeloid and lymphoid cells, have Young's moduli in the range of 0.1-0.2 kPa [112]. Less compliant or stiff cell types, such as osteoblasts and cardiomyocytes, can range between 2 and 10 kPa, with contracted muscle cells having reported moduli as high as 100 kPa [112]. Cross-study comparisons are complicated by a lack of standardization of experimental protocols and techniques. Therefore, studies that include cells from multiple tissues in their experimental design are often the best means to observe relative differences in mechanical properties. Darling et al. [19] have shown that superficial-zone chondrocytes are approximately twice as stiff as middle or deep zone chondrocytes (1.2 kPa versus 0.6 kPa, respectively).

They also reported values for spread and spherical human osteoblasts (6.5 kPa for spread cells; 2.6 kPa for spherical), chondrocytes (1.8 kPa; 1.4 kPa), adipocytes (0.9 kPa, spherical only), adipose-derived stem cells (2.5 kPa; 2.6 kPa), and bone-marrow-derived stem cells (3.2 kPa; 2.5 kPa). Azeloglu et al. [4]

characterized the mechanical properties of both nuclear and cytoplasmic regions for alveolar type I cells (2.5 kPa for nuclear; 2.5 kPa for cytoplasmic) and type II cells (3.1 kPa; 4.7 kPa) and lung fibroblasts (3.3 kPa; 6.0 kPa). The reason each of these cells exhibits a characteristic mechanical phenotype is largely associated with the biological role they fullfill. However, researchers can use these properties as a means to further identify a specific cell type, potentially for sorting or enrichment purposes, in analogy with tisue diagnosis, palpation has being used as diagnosis tool for ages. Red blood cells (RBCs) are a special case of somatic cell that has been extensively studied to determine mechanical phenotypes associated with health and disease [45, 83], with applications focused primarily on disease diagnosis rather than on cell purification.

Cell	Young's moduli [kPa]
Lymphoid	0.1 - 0.2
Myeloid	0.1 - 0.2
Osteoblast	2 - 10
Cardiomyocytes	2 - 10
Contracted Muscle	100
Spread osteoblast	6.5
Spherical osteoblast	2.6
Bone-marrow-derivered stem cells	2.5 - 3.2
Lung fibroblast	3.3 - 6
Red blood cells	1.5

TABLE 1.1. Young's modulus values for different somatic cells.

1.2.4.1 Red blod cells (RBC)

Healthy human Red Blood Cells (RBCs) have a biconcave shape with approximately 7.5-8.7 μm in diameter and 1.7-2.2 μm in thickness [35]. The RBC envelope consists of a phospholipid bilayer and a network of spectrin proteins (cytoskeleton) attached at the inner side of the bilayer via transmembrane proteins. The spectrin network supplies shear elasticity to a RBC membrane, while the lipid bilayer serves as a barrier for exchange of solutes and provides resistance to bending and viscous damping when sheared. Human RBCs neither have organelles nor bulk cytoskeleton and are filled with a highly concentrated hemoglobin solution. Viscosity of the cytosol is about 6×10^{-3} Pa·s, while the plasma viscosity is approximately 1.2×10^{-3} Pa·s at a physiological temperature of 37° C [23].

The unique structural organization of the RBC enables it to undergo large reversible deformations while maintaining constant volume and membrane surface area. Lacking the actin-myosin-microtubule cytoskeleton that is responsible for shape changes in nucleated cells, RBCs maintain their structural integrity and can display dynamic local deformations thanks to a dynamic network of spectrin filaments tethered to the cytosolic side of the Plasma Cell Membrane (PM) [29].

The RBC presents a Refractive Index (RI) of 1.3610±0.0002 for 656 nm red light [63]. Is not common find information about the optical properties of the cells, but RBCs are well know turning them into a good reference parameter for cell optical and physical parameters assessment.

1.2.5 Stem cells

During the past decade, researchers have focused intensively on how stem cells sense and respond to the mechanical properties of the materials around them. In the last few years, attention has also focused on the mechanical properties of stem cells themselves, particularly during differentiation. During this process, major changes occur in gene expression and protein abundance, resulting in similarly drastic changes in cytoskeletal structure and architecture. In fact, biological and mechanical factors often interact during differentiation, with the mechanical cues serving as a driving factor in embryonic development. Evaluating the mechanical properties of stem cells before, during, and after differentiation holds clues to what aspects are most important in controlling this unique behavior [21, 62].

1.3 Mechanical and optical label-free biomarkers

All cells express characteristic features (proteins, lipids, glycosylation, etc.) that can be used as markers to help distinguish unique cell types. Cell markers can be expressed both extracellularly on the cell's surface or as an intracellular molecule. Chemical markers are a powerful cytometry tool; for instance, molecular markers are highly selective. However, challenges still exist in terms of cost, complexity, and labeling heterogeneity. Therefore, demands for new tools are increasing to facilitate and accelerate unlabeled approaches for detecting biomarkers.

Fluorescent labels or chromophores are employed in some effective and available breast cancer biomarker detection methods that can provide exceptional sensitivity down to the single-molecule level. For instance, HER2 is a well-documented biomarker related to tumor cell proliferation with overexpression in 20-30% of human breast cancer [97].

Size, shape, and texture are potential mechanical markers for cells, which is the main feature intended to be exploited in this thesis. Hence, it is relevant to present the existing approaches for cell mechanotyping. Cell stiffness is a critical phenotypical marker that can provide insights into cellular adaptation and differentiation and pathological cell change. Therefore, cell-mechanical phenotyping contributes to biological research and medicine, including cell sorting and medical diagnostics [74].

Label-free cytometry devices have been used recently with great success in diagnostics. A compact and label-free optical fiber sensor based on a taper interferometer cascaded with a fiber Bragg grating are proposed by Sun et al. [97] to detect a breast cancer biomarker (HER2). The tapered fiber-optic interferometer is extremely sensitive to the ambient Refractive Index (RI). The sensor surface is functionalized to make it insensitive to RI changes of target different from the unlabeled biomarkers. The result shows that the proposed sensor presents a low limit-of-detection of 2 ng/mL, enabling its potential application in early breast cancer diagnosis.

Studies indicate that the cell mechanical phenotype might be an inherent biophysical marker of pluripotent stem cells. Cell reprogramming is a differentiation process during which cells continuously undergo phenotypical remodeling [103]. Changes in the mechanical phenotype of murine fetal neural progenitor cells (fNPCs) during reprogramming is used to induced pluripotent stem cells (iPSCs) [103]. fNPCs become progressively stiffer en route to pluripotency, and this stiffening is mirrored by iPSCs becoming more compliant during differentiation towards the neural lineage. Furthermore, it is shown that the mechanical phenotype of iPSCs is comparable with that of embryonic stem cells. These results suggest that the mechanical properties of cells are inherent to their developmental stage.

The physiological cell properties of interest for us are the mechanical properties and the optical properties. Regarding the last one, among the intrinsic optical biomarkers, the most representative is the RI, which has been successfully used for breast cancer diagnosis. Three types of unstained breast tissue sections, fibrocystic, fibroadenoma, and invasive carcinoma, have been examined for the ultrastructural changes using Fourier domain low coherence interferometry [7]. Structural changes occurring with malignancy occur as refractive index variations inside the tissue. It is crucial to quantify this variation in refractive index for early cancer detection. The resulting interference spectra of the backscattered light from the front and the rear surface of the sample are Fourier analyzed to provide depth correlation function. The subtle small-scale fluctuations in the Fourier analyzed spectra are then evaluated using

Discrete Wavelet Transform (DWT). Daubechies-1 wavelet of DWT is used to calculate the high-pass and low-pass coefficients. The sixth level low-pass coefficients of DWT discriminate among normal, benign, and malignant breast tissue. Other optical properties such as reflectivity of cells can be exploited as markers if they can be accurately determined for each type/state of the cells.

1.4 Techniques for measuring mechanical properties of single-cells

Nowadays several approaches exist for single cells mechanical properties assessment:Atomic Force Microscopy (AFM), Micropipette Aspiration (MA), Microbead Rheometry (MR), Cell Monolayer Rheology (CMR) and Optical Tweezers and Traps (OTs), see Fig. (1.6). The optimal choice of technique depends largely on the goal of the experiment. However, it should be kept in mind that each technique has its strengths and weaknesses, and some may introduce biasing due to the nature of the test. For example, MA and AFM can both be used to determine Young's modulus of a cell, but the former typically test cells in suspension, whereas the latter typically tests cells adhered to a surface. Even if cells in both cases exhibit a rounded morphology, the measured properties will be influenced significantly by underlying cytoskeletal differences i.e., surface-adhered cells tested by AFM appear less viscous than those in suspension tested by MA [19].

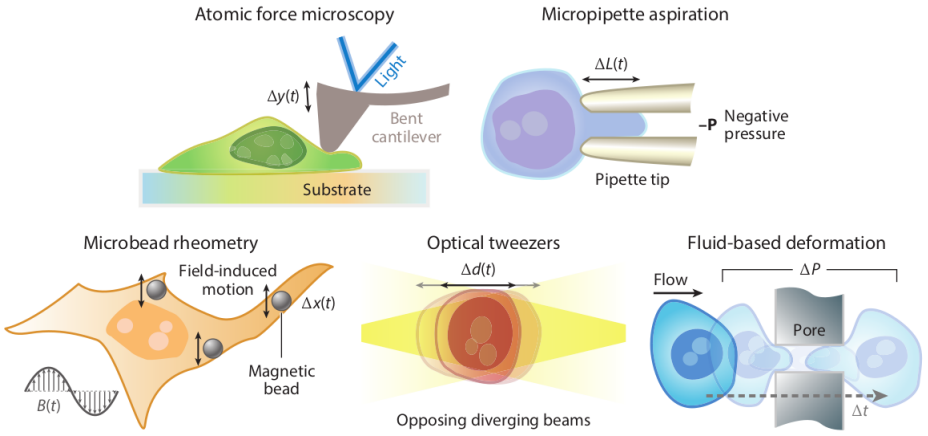

FIGURE 1.6. Traditional techniques that have been applied to measure the mechanical properties of cells. Taken from [21].

Likewise, a method that uses a tiny probe for indentation will acquire highly localized measures of mechanical properties. In comparison, a technique that deforms the entire cell will produce a different set of mechanical properties. The choice of method should be balanced against knowledge of a cell's architecture [19]. One way to avoid biasing the measurement of the mechanical properties would be a contactless method. High throughput would, in addition, be highly desirable.

1.4.1 Atomic Force Microscopy (AFM)

Monitoring the deformation of a cell in response to physical compression or indentation is one of the most common approaches to assay the mechanical properties of a single cell. AFM works on the principle of applying a force and monitoring the deformation response of a cell. From these data, elastic and viscoelastic properties can be extracted.

The vertical bending of a cantilever is measured with a laser, and the result is used to calculate an applied force at the tip, which is typically shaped as a sphere, cone, or pyramid. Although the selection

Technique	Cell restrictions	Mechanical properties	Force range	High throughput
Atomic force microscopy	Adherent cells	Elastic and viscoelastic properties of a local region or a whole cell	pN - μN	Potentially
Micropipette aspiration	Nonadherent or detached adherent cells	Elastic and viscoelastic properties of local region or a whole cell	pN - nN	Potentially
Microbead rheometry	Adherent cells	Elastic and viscoelastic properties of a local region	pN	No
Optical tweezers and traps	Adherent or nonadherent cells	Membrane elasticity, whole-cells deformability	fn - pN	Potentially
Fluid-based deformation cytometry	Nonadherent or detached, adherent cells	Whole-cell deformability	pN	Yes

TABLE 1.2. Summary of conventional approaches to testing single-cells. Taken from [21].

of cantilever stiffness and probe geometry are highly dependent on the design of the experiment, for whole-cell indentations, it is recommended to use a very soft cantilever (stiffness (k) approximately $0.01-0.06N/m$) and a spherical tip (approximately 5 μm). Empirically, indentations should be less than 10% of the cell diameter or height, and cantilever deflections signals should be reliably above noise levels in a fluid environment ($>5-10nm$) [92].

The most prevalent approach is to use the Hertz model with indentation data to determine Young's modulus. The choice of model, as well as the testing parameters, can dramatically influence the reported properties of a cell and should be carefully considered when making comparisons across studies [21, 65].

Tip Size	Temperature	Loading Rate [μm/s]	Elastic/Storage* modulus [kPa]
Conical probe	25°C	6	13.5±7.0
Conical probe	37°C	2	5.5±0.8
750 nm	37°C	2	0.58±0.23
2,500 nm	25°C	6	1.31±0.54
2,500 nm	37°C	10	0.53±0.52

TABLE 1.3. AFM elastic modulus for different measurement conditions and same type of cells. *Elastic moduli derived from AFM represent the effective Young's modulus. Taken from [111].

1.4.2 Micropipette Aspiration (MA)

This approach involves applying suction pressure to a cell while monitoring the extension of the membrane (and sometimes nucleus) using a micropipette. This technique has also been used for decades to study RBCs [83]. Like AFM, MA can be used to evaluate the viscoelastic properties of cells, both in local regions and as a whole-cell measurement. The choice of the micropipette's inner diameter s crucial to the validity of the theoretical equations used. Negative pressure is also critically important, since it controls how much of the cell is drawn into the micropipette. Small extensions (requiring approximately 1 Pa) primarily measure properties of the cell membrane, whereas large extensions (requiring approximately 1,000 Pa)

measure cytoskeletal and cytoplasmic properties. Cell nuclei, both alone and in living cells, have also been studied extensively using MA [83, 99, 88].

1.4.3 Microbead Rheometry (MR)

The test can evaluate elastic and viscoelastic properties in highly localized regions. Practically, this is accomplished by placing magnetic microbeads on or in a cell and monitoring their motion. The advantage of microbead rheometry over other techniques is that it can provide a very detailed description of the mechanical properties of a cell by interrogating multiple locations corresponding to multiple localized beads at one time. This is not feasible with AFM or MA. The major drawback is in the magnitude of forces that can be applied (piconewtons), limiting it to measuring local biological features [18, 105].

1.4.4 Cell Monolayer Rheology (CMR)

Cell Monolayer Rheology probes cells placed between two plates of a commercial rotational rheometer with a glass sensor and plate-ring geometry, which provides more accurate measurements in the regime of large shear deformations than the conventional plate-plate geometry. Fibronectin coating ($2\mu g/cm^2$) of the plates enhances cell adhesion; cells form a sparse monolayer that can be observed through a microscope during measurements. The ring rotates around its symmetry axis, which leads to simultaneous shear deformation of the cells [111].

In a similar approach, Huang et al. [50] present progress in quantifying traction forces generated during cell-ECM/substrate interaction, with an emphasis on force/stress reconstruction on functionalized ECM/substrates.

1.4.5 Optical approaches

1.4.6 Optical Tweezers and Traps (OTs)

Upon transmitting through a dielectric particle, the photons from the laser beam undergo a series of processes, including absorption, scattering, emission, and re-radiation, thus inducing momentum transfer in both the photons and the particle interacting with them. Therefore, an optical force that equals the time rate of momentum changes is exerted on the particle. The radiation force is generally divided into two components: the scattering force proportional to the incident light and the gradient force proportional to the intensity gradient. Under the gradient force, particles with a higher refractive index than the surrounding medium will be transported into the high-intensity region of the beam near the focus, whereas particles with a low refractive index will be pulled toward the low-intensity area. For dielectric particles in the geometric optics regime, where the particle size (diameter d) is large compared with the trapping wavelength ($d > \lambda$) [117].

Light-based cell-manipulation approaches, including optical tweezers and traps (known as OTs), are attractive testing methods that do not require mechanical contact with the cells under examination. The basic principle of laser traps is that momentum is transferred from the light to the object, which in turn, by Newton's second law, exerts a force on the object [40, 41]. OTs use a highly focused laser beam to create a 3D light gradient that exerts attractive and repulsive forces on a bead or cell, relying on a dielectric

contrast with the surrounding solution [2, 3]. One of the limitations of using OTs for measuring the properties of single cells is the relatively small-magnitude force that can be applied, typically less than a couple of hundred piconewtons. In addition, the high intensity needed for trapping at the focussed spot, in excess of (MW/cm^2), introduces potential thermal damage to cells RBCs included [117].

The most common laser trap is a one-beam gradient trap, called optical tweezers. Its configuration is stable as long as the gradient force overcomes the radiation pressure. In principle, the one-beam trap can use a spot size smaller than the sample cell. In contrast, the optical stretcher is based on a double-beam trap. Two opposed, slightly divergent, and identical laser beams with Gaussian intensity profile trap an object in the middle. This trapping is stable if the total force on the object is zero and restoring. This condition is fulfilled if the refractive index of the object is larger than the refractive index of the surrounding medium and if the beam sizes are larger than the size of the trapped object [40].

Forces applied by OTs have also been adapted for higher-throughput measurements like the microfluidic optical stretcher. Practically, these approaches all stretch cells directly with optical forces rather than with pairs of beads attached to cells because such bead-attached cells are a statistical minority in a population. The optical stretcher is the first approach to make a significant advance [41], achieving a throughput of approximately 1 cell/min, mainly limited by the need to wait for a sufficient time to image small, creeping cellular deformations.

1.5 Acoustic approaches for single-cell mechanotyping

Acoustic manipulation of cell is implemented in the device developed in this thesis. In combination with interferometry, the cell deformability in a high throughput fashion is addressed. Here is presented the progress already achieved in cell acoustic manipulation such as acoustophoresis and cell acoustic deformation. Both techniques are incorporated into our technology.

Standing acoustic waves have only recently been coupled to a microfluidic (planar resonator) cavity to yield forces on cells that depend on the relative compressibility and density of the cell compared with the surrounding fluid. By following the trajectories of cells in this standing acoustic wave, cancer cell lines were determined to have a compressibility of $> 4.0 \times 10^{-10} Pa^{-1}$, while nonmalignant cells had $< 4.0 \times 10^{-10} Pa^{-1}$ [43]. This technique was able to process approximately 300 cells/s, suggesting that it could be applicable for rapid cell analysis.

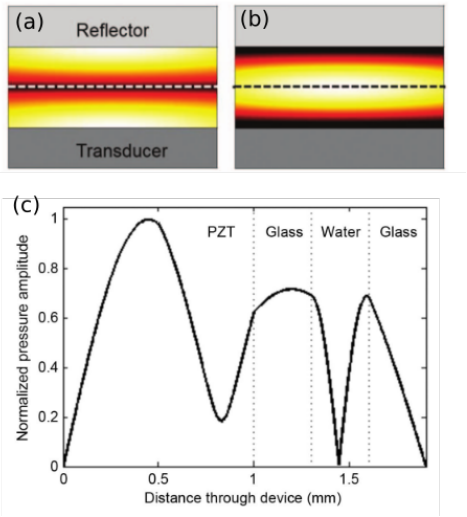

FIGURE 1.7. Example of acoustic field distributions: (a) pressure magnitude and (b) velocity magnitude, in a resonant cavity, with a stronger field near the center of the cavity. Arbitrary linear scale: light: 1, dark: 0. (c) Normalized pressure distribution through the thickness of the device from 1-D simulation. Adapted from [38].

An ultrasonic standing wave field is created in a 0.1 mm glass capillary at a frequency of 7.9 MHz to deform cells. The reported deformations in osmotically swollen red-blood cells are up to an aspect ratio of 1.35 [75]. The applied acoustic pressure varies from 12.9 kPa to 978 kPa. The resulting acoustic standing wave is dominated by planar variations in pressure, causing particles to migrate to planar pressure nodes or antinodes depending on particle and fluid properties [37].

In a macroscopic approach use of acoustic levitation to study normoxic (normal level of oxygen) rheological properties of normal and Sickle Cell Disease (SCD) blood has been exploited [47]. A drop of whole blood is levitated in an acoustic field and excited to modal shape oscillation by amplitude modulation of the field. The free decay of the shape oscillation is measured using a laser scattering method, from which blood viscosity is inferred. Correlation of the measured viscosity with clinically measured parameters for

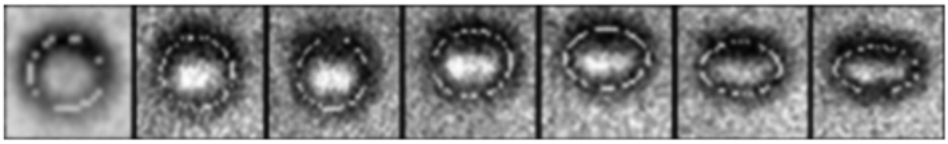

FIGURE 1.8. Images showing a single osmotically swollen red blood cell under the influence of a range of acoustic pressure amplitudes from 0-978 kPa. Some relevant parameters: cell density 1 = 139 kg m^{-3}, cell membrane Young's modulus = 629 Pa, frequency 7.9 MHz, speed of sound in cell 1680 m/s, speed of sound in medium = 1480 m/s, cell membrane Poisson's ratio = 0.499. Taken from [75].

SCD patients, this technique can provide insights into the disease pathophysiology and the effectiveness of hydroxyurea treatment. In particular, the results show that hydroxyurea treatment reduces whole blood viscosity, and further that this viscosity reduction correlates with fetal hemoglobin production while exhibiting no correlation with mean corpuscular volume.

Finally, microfluidic acoustophoresis has been used in many applications involving contactless cell and particle manipulation, separation, and concentration [110]. There are mainly two types of microfluidic acoustic cell manipulation approaches, those using bulk acoustic wave resonators and those using Surface Acoustic Wave (SAW) resonators. Although SAW-based acoustofluidic devices have been extensively employed for cell and particle separation, so far, SAW resonators are not suitable for direct single-cell mechanotyping studies. Besides, this method requires expensive specialized substrates and more complex fabrication procedures.

Attaching a piezoelectric transducer to the bottom of a simple microfluidic channel can perform acoustophoresis cytometry Fig. (1.9). Introducing the cells into the acoustic field at a constant position and recording their exit positions after acoustophoretic displacement a continuous-flow acoustofluidic cytometer was achieved, this configuration allows for a decoupling on the size-dependent effect from the compressibility-dependent effect given that the cells would experience different acoustophoretic forces and acoustic streaming depending on their initial vertical locations [110].

The first-order resonance frequency corresponding to the channel width (the correspondent frequency of the wave whose length is precisely twice the channel width) was applied to generate a transversal (Y-direction) acoustic resonance field in the microchannel. As cells entered the acoustic field, they were subject to the acoustophoretic force, which moved them to the transversal first harmonics pressure node in the channel center, as well as to the size-dependent viscous drag force that was applied in the opposite direction. By tuning the acoustic pressure field (adjusted by the applied power) and cell transit time (adjusted by the flow rate), the transversal positions of cells when exiting the acoustic field could be controlled in the range between the channel sidewall and channel center. In this way, only cells with a higher acoustic contrast factor move closer to the center pressure node, while cells with a lower contrast factor do not have enough time to move to the center pressure node. This allows relating the cells' transversal position differences to the acoustophoretic force differences caused by their size, density, and compressibility differences.

This acoustophoresis cytometry technique has been applied for single-cell mechanotyping of two different types of cancer cells [110] by using two microfluidic devices. The first set of fabricated microdevices

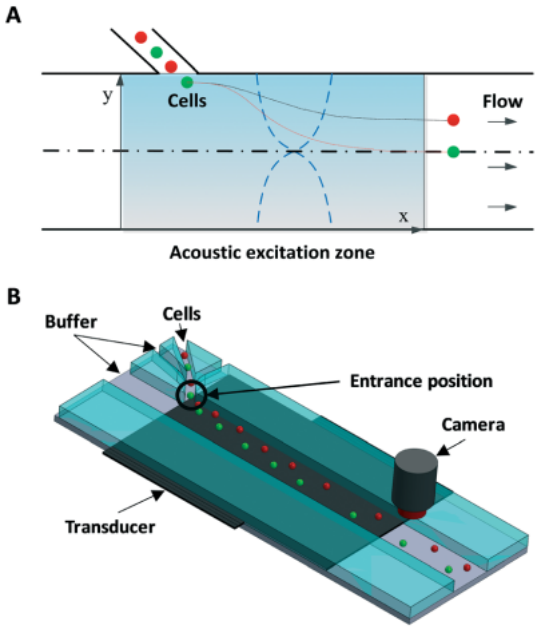

FIGURE 1.9. Working principle and schematic illustration of the acoustofluidic cytometer. (A) Cells are introduced from the side inlet into the acoustic resonance field, where cells with different biophysical properties (such as size, density and compressibility) experience different acoustophoretic forces while passing through the acoustic resonance field, and therefore exit at different Y-positions. Red spheres indicate cells that have a smaller acoustic contrast factor compared to the cells shown as green spheres. (B) The proposed system consists of a three-inlet side channel that allows flow-focused cells to be introduced into the main straight channel where the acoustic resonance field is applied using a piezoelectric transducer attached to the bottom of the device. A camera records the exit position. Taken from [110].

had a main microchannel width of 370 μm and a side-channel width of 30 μm. The second set of fabricated microdevices had the main microchannel width of 390 μm and a side-channel width of 38 μm. The flow rates in each stream were set to: center main inlet 100 μl/h, side inlet 10 μl/h, and side sheath flow inlet 10 μl/h. The acoustic resonance field was generated using a piezoelectric ceramic plate (PZ26, Ferroperm Piezoceramics A/S, Denmark) attached to the bottom, which was stimulated with a sinusoidal wave of 2.17 MHz for set 1 and 1.835 MHz for set 2, respectively, amplified using a 50 dB power amplifier.

Three different breast cancer cell lines were testes in the set 1 microdevice, see Fig (1.10), BT-474, MDA-MB-231, and MCF7, as well as immortalized breast epithelial cell line MCF-10A. BT-474 is a ductal carcinoma cell line with primary tumor origins, while MCF7 and MDA-MB-231 are also ductal carcinoma cell lines but derived from metastatic sites by pleural effusion. While in the set 2 microdevice the compressibility of three head and neck cancer cell lines cl-37B, M4e and Tu686 were evaluated.

MDA-MB-231 has been reported to be significantly more invasive than MCF7, which translates to a higher compressibility and acoustic contrast factor, and indeed move more towards the channel center compared to MCF-7. reported a higher compressibility of MCF7 cells, compared to MCF-10A,

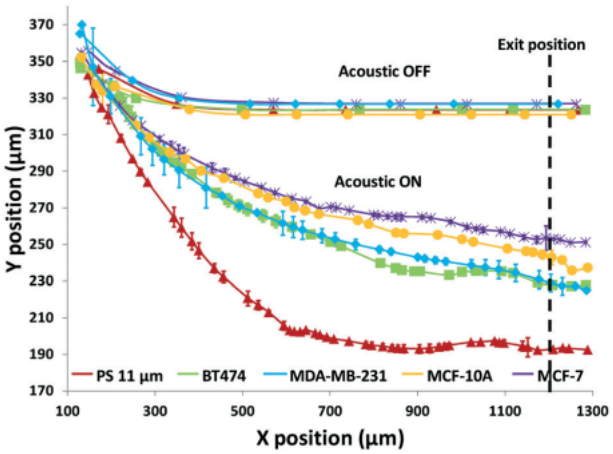

FIGURE 1.10. Trajectories of 3 different breast cancer cell lines; BT-474, MDA-MB-231, MCF7, along with two breast epithelial cell lines BT-474, MCF-10A, and 11 μm polystyrene beads (PS) as controls, measured using the developed acoustofluidic cytometer. Error bars show the standard deviation of 6 trajectories of each particle per cell type. The dashed line indicates the measurement location of the cells' exit Y-position at X = 1200 μm. Taken from [110].

in contradiction with this result. This is an indicator that trajectory analysis alone cannot accurately determine cell compressibility-dependent movement, since other parameters such as cell size also play a role. Therefore it is necessary to decouple the cell size-dependent effect from the cell compressibility-dependent effect.

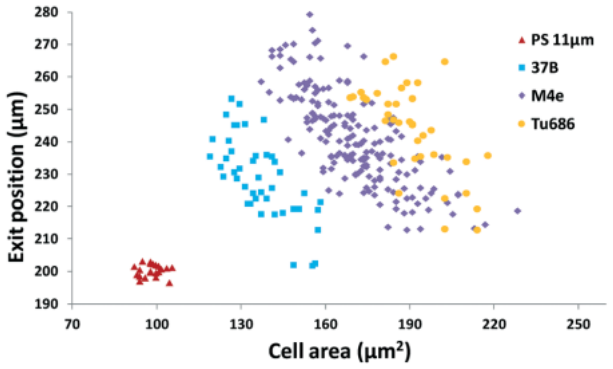

FIGURE 1.11. Scatter plot of the cell size (in the form of cross-sectional cell area) and cell exit position (Y-direction) of head and neck cancer cell lines to quantify and group the cells based on their different biophysical properties. (n = 290). Taken from [110].

By including the cells' size in their analysis, it is possible to increase the accuracy of the measurements proving, for instance, that MDA-MB-231 shows a longer traveling distance in the transversal direction, which can be interpreted as MDA-MB-231 experiencing a stronger acoustophoretic force and similar

drag force, an indicator of a higher acoustic contrast factor. It was also shown that cell lines could be successfully distinguished using this scatter plot (see Fig. (1.11)). The order of the acoustic contrast factors of the head and neck cancer cell lines was cl-37B (0.235 ± 0.048) > M4e (0.153 ± 0.026) > Tu686 (0.133 ± 0.025). When no acoustophoretic force was applied, all cells showed the same exit position as expected. When the acoustophoretic force was applied, a simple exit position-based classification showed the order BT474/MDA-MB-231 > MCF-10A > MCF7, with no obvious differences between BT474 and MDA-MB-231. From the previous experiment, the relevance for taking into account the cell size becomes clear when performing a deformability-based cytometry study.

As exemplified before in the AFM section, cell deformability studies can be biased mainly due to how the load force is applied. Important efforts to properly asset this biasing, both experimentally and theoretically, have to be implemented. Contactless approaches for deformability cytometry will reduce such biasing, facilitating the technique and potentially leading to a substantial throughput.

1.6 High-throughput techniques

To compensate for the heterogeneous nature of biological materials, a high-throughput method to assess the mechanical properties of individual cells is required [26]. Reliable information can only be gained from sufficient statistics. Thus thousands to million cells need to be processed over periods that range from minutes to, at most, hours. The most demanding application scenario is clinical analysis, in which throughput of 100s to 1000s of cells per second is foreseen. In addition, a short processing time is valuable to minimize the physical changes that can occur as cells sit in buffer or media before processing. Even higher throughputs might be needed to prepare therapeutic batches of cells containing hundreds of millions of cells [21].

1.6.1 Real-time Deformability Cytometry (RT-DC)

RT-DC is a contactless technique, allowing the gain of thousands of events per minute, convenient for the global characterization of complex samples. In the RT-DC set-up, shear stress is generated by a viscous liquid flowing through a channel of defined dimensions to induce cell deformation [42].

Cells are flowed through a microfluidic channel constriction and deformed without contact by shear stresses and pressure gradients. The deformed cell inside the constriction is illuminated with a pulsed, high-power LED and imaged with a complementary metal-oxide-semiconductor (CMOS) camera at 2,000-4,000 f.p.s. The camera-triggered LED light pulses are 1 μs in duration-short enough to prevent motion blurring of the cells, which flow with 10 cm/s and deform from a spherical into a bullet-like shape.

Real-Time Deformability Cytometry (RT-DC) is a technique for continuous cell mechanical characterization of large populations (> 100,000 cells) with analysis rates greater than 100 cells/s. RT-DC is sensitive to cytoskeletal alterations and can distinguish cell-cycle phases, track stem cell differentiation into distinct lineages and identify cell populations in whole blood by their mechanical fingerprints. An image analysis algorithm is applied and executed on a standard personal computer that continuously acquires images from the camera in real-time, detecting the presence of a cell and determining its contour, quantifying its deformation and size [76, 78, 102]. This technique adds a new label-free dimension to flow cytometry with diverse biology applications, biotechnology and medicine [74].

One application of the RT-DC is the in vitro manufacture of RBCs CD34+ from hematopoietic stem cells (CD34+) monitoring, since the in vitro protocol is a recapitulation of in vivo erythropoiesis through distinct developmental stages, induces mechanical changes in the cells. Initially, the culture is expanded for the first ten days (D0 to D10) before differentiation is induced at D11, resulting in drastic cell phenotype changes during the final 11 days of differentiation. Guzniaczak et al. used a microfluidic-based Real-Time Deformability Cytometry (RT-DC) to track the evolution of the mRBCs during its developmental stages [42].

However, this very sensitive, label-free technique (RT-DC) still lacks the specificity of molecular markers. Rosendahl et al. [85] developed an approach that combines real-time 1D-imaging fluorescence and deformability cytometry in one instrument: Real-time fluorescence and deformability cytometry.

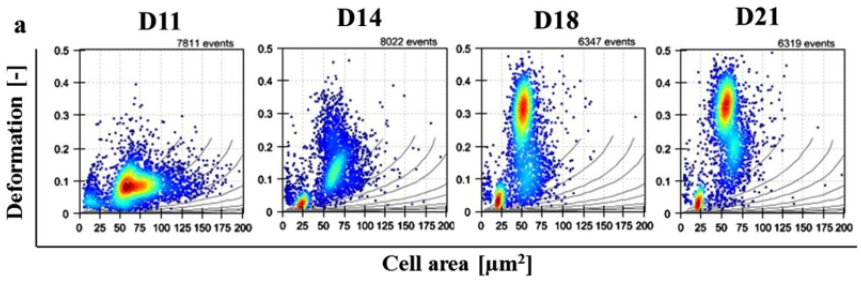

FIGURE 1.12. Scatterplots obtained from RT-DC for CD34+ undergoing in vitro haematopoiesis corresponding to four time points: D11, D14, D18 and D21. Cells are flowing at 0.12 μl/min through a 20 μm × 20 μm channel. Colours indicate a density scale. Taken from [42].

1.6.2 Transit through constrictions

Transit through constrictions is perhaps the simplest method of assaying the deformability of cells in a high-throughput. The cell is forced to flow through a microfluidic channel with constrictions and measuring the transit time. Recent efforts have also aimed at decoupling cell-deformation time during entry into the constriction, which requires the entire cell to change shape from transit time following deformation, which may depend more on elastic restoring forces and surface friction within the channel [12]. Analyses of 1 cell/s [12]. to approximately 100 cells/s [116] have been demonstrated using significant automation see fig (1.13).

(a) network of bifurcating microfluidic channels for blood cell deformability

(b) microfluidic system for electrical and mechanical characterization of RBCs

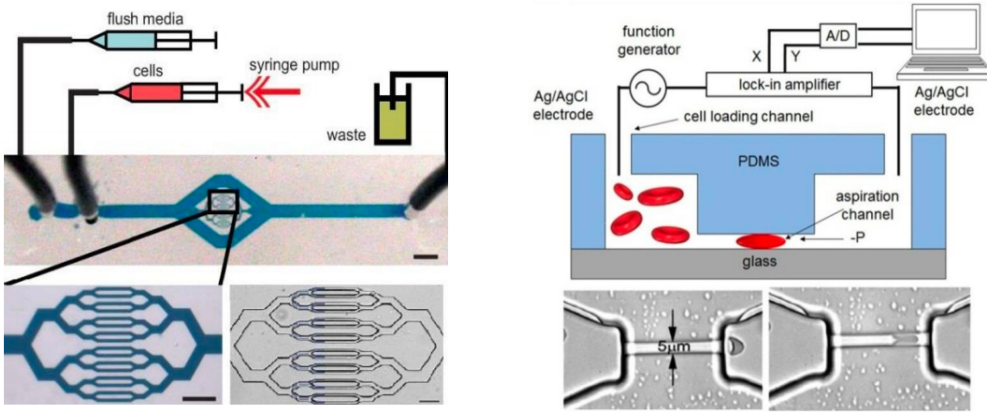

FIGURE 1.13. (a) A network of bifurcating microfluidic channels for blood cell deformability measurement. The transit time of the individual cells are measured using a high-speed camera. (b) A microfluidic system for electrical and mechanical characterization of RBCs at a speed of 100-150 cells/sec. Adapted from [116].

1.6.3 Fluid-Based deformation cytometry

By tethering the cell to the channel wall, uniaxial stretching could be applied to measure the elasticity of the cell membrane. When used in combination with finite-element modeling, measurements of mechanical properties have similar precision to techniques such as AFM, MA, and OTs [82]. Fluid-based deformation techniques are currently limited in the types of mechanical properties that they can measure and the accuracy of those measurements but offer high throughput.

1.6.4 Hydrodynamic approaches

Hydrodynamic approaches separate cells and measure their mechanical properties by using intrinsic fluid-dynamic stresses tuned by the microfluidic channels' design. The two main classes of hydrodynamic approaches rely on (a) deformability-induced lift to cause the lateral migration of cells in a continuous flow and, therefore, achieve deformability-based separation and (b) hydrodynamic cell stretching and imaging in extensional microfluidic flows in which strain in a controlled hydrodynamic stress field is measured by high-speed microscopy

This lift force can be directly used and balanced against other hydrodynamic lift forces in the dilute limit to separate cells based on deformability [52] see Fig. (1.14). At higher cellular-volume fractions in the blood (approximately 40-50%), deformable RBCs migrate preferentially to the center of the channel and exclude, for example, stiffer malaria-infected RBCs or WBCs through a process called margination. Margination has been used to enrich WBCs from blood [91] and concentrate RBCs with malarial parasites [91].

Hydrodynamic approaches yield the highest throughputs of any current technique (up to 20,000 cells/s) [28]; however, the stress field acting on a cell in a microflow depends on cell size and shape, the measurements are sensitive to these parameters.

1.6.5 Automated Atomic Force Microscopy

The automation and parallelization of AFM instrumentation have been proposed to achieve higher-throughput measurements of cell mechanics. Yuan and coworkers [110] have developed an automated system that includes feeding back information from the analysis of microscopic images to enable automatic positioning and indenting. This level of automation still requires several seconds per measurement due to the nature of the indentation process, suggesting that parallelization is necessary to achieve more practical measurement throughput. An arrayed implementation has also been designed for the purpose of measuring cells that are pre-patterned on a substrate [32]. In this approach, a 4×17 cantilever-probe array was fabricated to register with a patterned array of cells. An interferometric readout scheme was implemented using a standard CMOS. to parallelize the accurate position sensing of the different probe tips, instead of measuring laser deflection.

1.6.6 Osmotic approaches

Another method of applying stress to a cell, although focused on the cell membrane, is through osmotic shock. Historical techniques have used such an approach to characterize membrane integrity and cortical cytoskeletal strength, especially in RBCs [51]. These early osmotic fragility tests characterized the quantity

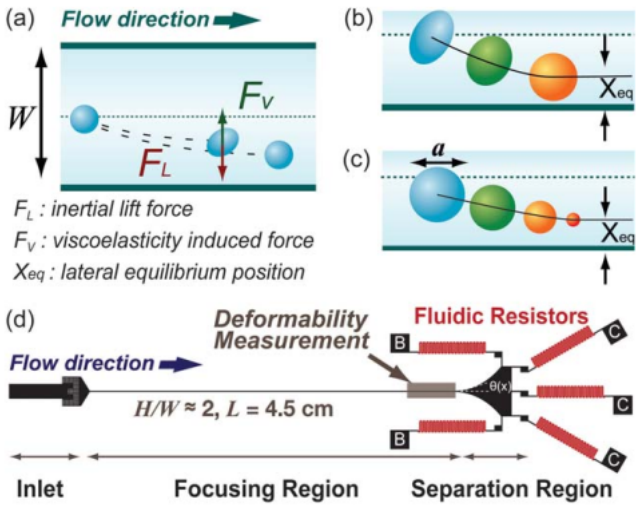

FIGURE 1.14. Classifying and separating cells and particles by deformability. (a) The balance between two lateral forces, namely inertial lift force, F_L, and viscoelasticity induced force F_v, leads to unique lateral inertial focusing equilibrium positions X_{eq}, for (b) deformable particles and (c) rigid particles with various diameters, (d) The microfluidic device used for cancer cell enrichment based on these parameters consists of an inlet with a coarse filter, a straight focusing (40 × 93 mm) region, and a gradually expanding separation region ending in 5 branched outlets with high fluidic resistance. Outlets, denoted as B or C, represent the designated collection outlets for blood cells and cancer cells, respectively in enrichment experiments. All schematics represent the top view of the microfluidic device. Taken from [52].

of cells lysed at a given time using bulk absorption measurements of hemoglobin or measures of intact pellet size after centrifugation. More recently, individual cells undergoing lysis have been tracked using video microscopy to study osmotic fragility in RBCs in a static setting [54]. The approaches taken to increase the throughput of osmotic fragility tests make use of microfluidic devices that create osmotic shock by either electroporation [6] or exposure to a hypotonic solution [114]. Following membrane disruption or hypotonic exposure, RBCs gradually lyse and lose contrast as the index of refraction of the internal cytoplasm begins to match that of the external fluid, and this can be imaged with a high-speed camera. Single cells can be tracked using some approaches, and the lysis time can be determined quantitatively. Because of the serial and continuous nature of the assay, thousands of cells can be analyzed in a reasonable period at rates of approximately 1 cell/s [6].

1.7 Motivation

Although many approaches for assessing the physiological properties of cells exist, both using chemical markers and label-free, there is still a need to develop further technology that is reliable, fast, simple, and inexpensive.

As shown in table 1.2, the current methods to determine cell mechanical properties are largely biased due to the used technique. The immediate way to increase the robustness of the method would be by providing statistical analysis, and for such purpose, high throughput is needed. Nevertheless, high throughput methods require specific elements, like high-speed cameras, turning them into expensive or complicated approaches.

Having technology for single-cell phenotyping with high throughput but inexpensive and straightforward is highly desirable. It will have application in diagnosis, especially in the most vulnerable sectors of the society like the communities in the developing countries.

The goal of the technology presented in detail in the following pages is to provide a device for single-cell phenotyping analysis achieving high throughput, but keeping it simple, susceptible of miniaturization, cheap, and specially intended for diagnosis but with a broad spectrum of applications like cell sorting, medical treatments, drug test, cells developing monitoring, and even with applications out of the medicine and biophysics fields like water or air contaminants detection and measurement.

1.8 Chapter summary

A review of the Fabry-Perot interferometry theory is presented in section 1.1.1, with particular emphasis, for the rest of the manuscript, on the Airy transmission function (cf. eqs. (1.14), (1.15) and Fig.(1.2)), the Full-Width at Half-Maximum (cf. eq. (1.21)), the Free Spectral Range (cf. eq. (1.17)) and the Finesse (cf. eq. (1.19)). The Finesse is one of the parameters that will be used to characterize the optomechanical properties of cells (cf. section 3.1.3). Some interferometric applications follow the overview of the Fabry-Perot theory in microscopy and cell and tissue studies. See sections 1.1.2 - 1.1.4.

Section 1.2 of this chapter offers a detailed discussion of the Mechanical Properties of single cells. The designation "single" is important here since the mechanical properties of cells in tissue and single are different (often opposite) as in the case of cancerous tumors where the single cells are more elastically complaint than their healthy counterpart while the actual tumor is stiffer than the surrounding tissue. Among all the cell's organelles, the cytoskeleton is the one that plays a central role in controlling the mechanical properties of cells (cf. section 1.2). Cell mechanical properties are central to this work since they can be used as label-free biomarkers together with cell optical properties) to perform cytometry and clinical diagnosis (cf. section (1.3)).

A detailed review of the current techniques to assess the mechanical properties of cells presented in two separate sections: standard throughput (cf. section (1.4)) and high throughput (cf. section (1.6)). Interposed between these two sections is a review of the acoustic approaches for assessing cell mechanical properties (cf. section 1.5), an aspect highly relevant for this thesis. The analysis of state of the art in the measurement of cell mechanical properties highlights two particularly important needs: 1. standardization of cell mechanical property measurements and 2. the acquisition of large datasamples for statistical

analysis. The first need emerges from the variability in the measured parameter values, depending on the technique employed. The second one, from the fact that living systems, including cells, are extremely complex and therefore show a very high variability in their properties. As recent work in the field has shown, significant markers can be obtained only by analyzing large datasamples to extract average properties and statistical distributions. This constraint requires the availability of instruments capable of acquiring such large datasets, a feat which is only rarely accomplished with the current mechanical instrumentation.

One of the most used techniques to assess the cell mechanical properties is AFM; nevertheless, this technique reports different mechanical properties for the same cells. The reason lies in the construction of the tip used to deform the cell membrane. Given that a relatively large surface of contact develops during deformation, the shape of the AFM tip (sphere, pyramid, etc.) affects the result. This is regularly observed despite the use of mathematical models that try to extract information based on the tip's shape. On the other hand, each probe tip has its specific advantages and disadvantages, and different shapes must be chosen to match the kind of information to be retrieved (cf. section 1.6). The consequence is that widely different results can be obtained for the same cell (and even more when analyzing different cells). Thus, to the intrinsic cellular variability, the measurement adds an instrumental effect that complicates the results' interpretation. This problem holds for all mechanically-based measurement devices, such as, micropipette aspiration. Therefore the contactless deformation offered by the acoustic pressure, coupled to a non-invasive optical measurement, holds a high potential for standardization, given the lack of the constraint-induced by the mechanical contact introduced by the traditional methods.

High throughput is generally difficult to achieve with mechanically-based techniques; the typical yield with AFM or micropipette aspiration lies in units or, at best, few tens of units per hour (cf. section 1.6). Such rates are not conducive to the obtention of sufficiently large samples for statistical purposes. Neither can they be envisaged for medical diagnostic applications, where the number of cells to survey, to detect an illness in its early stages is enormous (easily in the millions). On the contrary, the Acoustofluidic Interferometric Device, thanks to its microfluidic base, is, potentially, capable of throughputs in the range of 100 cells/s when coupled to real-time analysis (as a future development cf. section 4.2).

CHAPTER 2

EXPERIMENT

This chapter is divided into two main sections. The first one (sect. (2.1)) presents materials and methods wherein a detailed description of the Acoustofluidic Interferometric Device (AID) components and operation is offered. In the second part (sects. 2.2-2.4), an analysis of the Gaussian beam behavior inside the FP interferometer and its relation with the Finesse and the spot size (strong cell perturbation region) is presented. Next, two possible FP resonator experimental configurations based on mirror separation and the Finesse are discussed to conclude that the large-gap Fabry-Perot with low Finesse configuration is the more suitable for our AID. Finally, a ray-matrix mathematical model to compute the Cell Focal Length (CFL) in the low Finesse FP large-gap configuration, with its error propagation, is presented.

2.1 Experimental Device

The experimental device developed for Acoustofluidic Interferometric Cytometry (AIC) comprises a microfluidic channel wherein a forced cell flow traverses the Fabry-Perot interferometer. In addition, the device is endowed with a cell acoustic manipulation system see Fig. (2.1). For this purpose, the microfluidic channel is equipped with a piezoelectric transducer that allows for cell acoustic focusing and deformation. After the standing wave is switched on, the focussed cells move in a single plane at constant speed. When flowing along the channel, the cells will traverse the (plano-planar) Fabry-Perot's illuminated region where the cell's presence perturbs the interference generated by the counterpropagating waves. The interferometer's fringe pattern, perturbed by the cell, is retrieved through the microscope objective – also used to couple light into the resonator – and is redirected to the detection unit Fig. (2.4) where the fringe pattern can be either stored as an image or be processed in real-time.

2.1.1 Acoustofluidic Interferometric AI chip

The microfluidic chip used in this work is based on a previously proposed geometry [37, 118]. One layer of double-sided adhesive transfer tape sheet (468MP, 3M, USA) is used as bond film 106 μm thick. The joined bond film is laser-cut into 35 × 50 mm pieces with a 5 mm wide microfluidic channel. The cut pieces are

sandwiched between two microscope slides (standard 170 μm thick, 25 × 75 mm) to create the microfluidic channel walls; a standard, fully reflecting mirror is attached to the back microscope slide. Access holes to the microchannel of 1 mm diameter were drilled at both ends of the channel, see Fig. (2.1) and [37].

Under a portion of the fluid channel, a piezoelectric transducer of lead zirconate titanate (PZ-26, Ferroperm, Kvistgaard, Denmark) is attached with epoxy (Epotek-301, Epoxy Technology, Inc., USA). The size of the transducer is (1mm x 25mm x 35mm), and a wrap-around electrode is created on the top surface, in contact with the glass, using conductive silver paint (SCP Silver Conductive Paint, Electrolube Ltd., UK).

A Direct Digital Synthesizer (DDS) AD9850 drives the piezoelectric transducer and is controlled by a Raspberry Pi 3 in conjunction with a custom-built amplifier based on a high-frequency op-amp. The driving frequency is is tuned at the microfluidic's channel fundamental acoustic mode resonance (6.682 MHz) with amplitude 15 V_{pp} for acoustic focussing and at 25 V_{pp} to induce cell deformation, see (2.2).

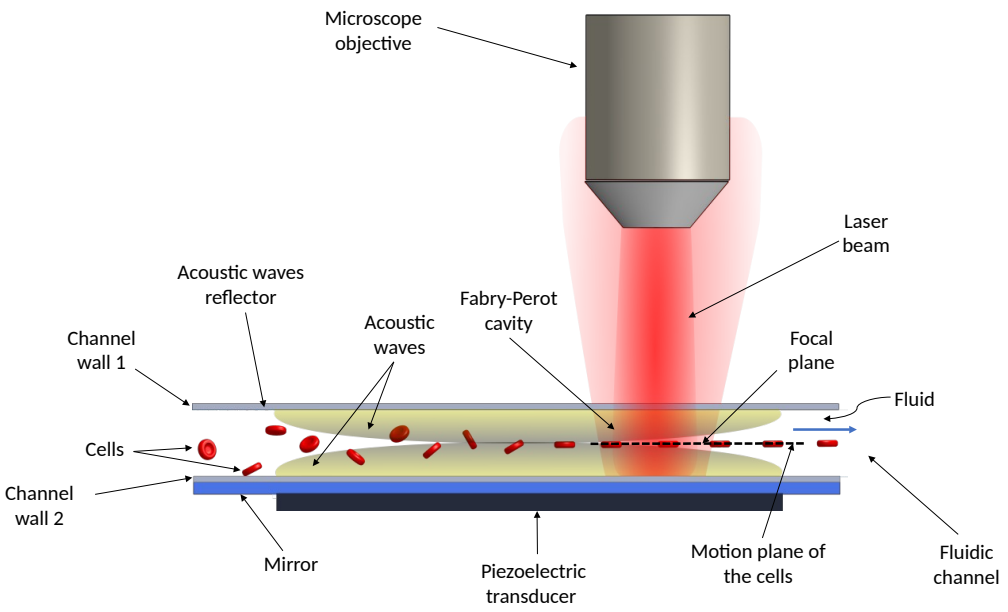

FIGURE 2.1. Elements of the microfluidic channel producing acoustic manipulation, together with a sketch of the Fabry-Perot resonator used for cytometry. The upper microfluidic channel wall (wall 1) serves as an acoustic reflector and, in addition, as one of the semi-reflective surfaces (mirror equivalent) of the Fabry-Perot interferometer. A piece of household mirror is sandwiched between channel wall 2 and the piezoelectric transducer to complete the interferometer. Light is coupled into the resonator using a microscope objective, also used to retrieve the interferometer fringe pattern with the imprinted, cell-induced fringe perturbation. The piezoelectric transducer creates the acoustic waves (yellow to black gradient) to focus the cells (red blood cells in the schematics) into a single motion plane.

Channel wall 1 serves as an acoustic reflector and one of the Fabry-Perot interferometer's reflective optical surfaces. The second reflective surface is the household mirror sandwiched between the piezoelectric transducer and the channel wall 2. A Thorlabs linearly polarized HNLS008L-EC He-Ne laser is focused inside the microfluidic channel with a microscope objective Olympus PLN 20X NA 0.40, Plan Achromatic, conjugated at infinity. The objective also serves to retrieve the Resonator Fringe Pattern (RFP) from the AID chip.

The air-wall 1 interface has a reflectivity of 0.04, while the back mirror provides a reflectivity of 0.9. Using eq. (1.11) we calculate the coefficient of finesse to 0.15 and, through eq. (1.19), we obtain a Finesse $\mathscr{F} = 0.6$. This value is quite low (F ranges above 10 and usually even above 100 in common interferometers), whence the identification "low-Finesse" for our device.

A hydrostatic pressure system is created using a pair of 10 ml syringes, and syringe tubing to induce and control the flow inside the microfluidic channel. This system allows us to generate pressures between 100 and 3000 Pa to cause cell speeds in the range 50-180 μm/s. However, the most common operation values used in experiments are 16 μl/min flow rate, i.e., an equivalent speed of 60 μm/s.

2.1.2 Resonance frequency

The sound frequency, ν_s, in the channel is defined by the dispersion relation $v = \lambda_s \nu_s$, where v is the speed of sound in water, and λ_s the corresponding wavelength.

The channel's fundamental resonance frequency ν_R is where λ_s are equal to twice the channel height. When driven at this frequency value, the channel's impedance grows, as the energy is more effectively transferred to the acoustofluidic chip. Consequently, the current provided by the power supply drops, inducing a reduction in the V_{pp} voltage measured by the oscilloscope. This small voltage reduction is used to identify the resonance frequency of the acoustofluidic chip (cf. Fig. (2.2)).

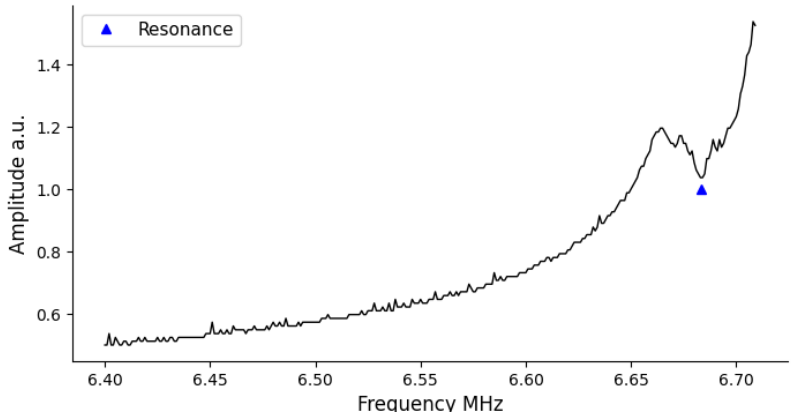

FIGURE 2.2. Response of the acoustofluidic chip to a frequency sweep. The acoustic chip's resonance frequency is 6.683 MHz and was determined by the local drop in the drive voltage of the piezoelectric transducer.

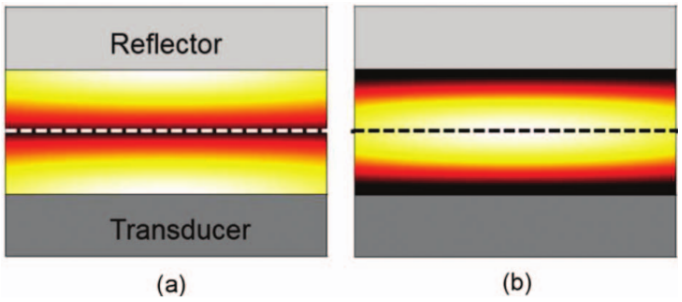

FIGURE 2.3. Example of acoustic field distributions: (a) pressure magnitude and (b) velocity magnitude, in a resonant cavity, with a stronger field near the center of the cavity. Arbitrary linear scale: light: 1, dark: 0. Taken from [118].

When the resonance frequency ν_R is matched, the standing wave produces potential acoustic energy that focuses the cells in a single plane (cf. Fig.(2.3)). The radiation force exerted on a compressible sphere, calculated for an arbitrary standing wave field, expressed by the time-averaged force, F, as a function of the gradients of the time-averaged kinetic and potential energy densities of the standing wave field is [118]:

$$F = -\nabla \left[\left(1 - \frac{\rho_f c_f^2}{\rho_p c_p^2} \right) \langle E_{pot} \rangle - \left(\frac{3(\rho_p - \rho_f)}{2\rho_p + \rho_f} \right) \langle E_{kin} \rangle \right] V , \tag{2.1}$$

where V is the particle volume, ρ_f and ρ_p are the densities of the fluid and particle, respectively, and c_f and c_p are the speeds of sound in the fluid and particle. The time-averaged kinetic and potential energy densities are related to the acoustic pressure field p and acoustic velocity magnitude u by

$$E_{pot} = \frac{1}{2\rho_f c_f^2} p^2 , \tag{2.2}$$

$$E_{kin} = \frac{1}{2} \rho_f u^2 . \tag{2.3}$$

Hence, a less compressible particle than the fluid will experience a component of force toward the potential energy density minimum and a particle that is denser than its surrounding fluid will experience a component of force toward the kinetic energy density maximum. Cells will undergo a more significant contribution from the potential energy term than from the kinetic term [118].

2.1.3 Detection unit

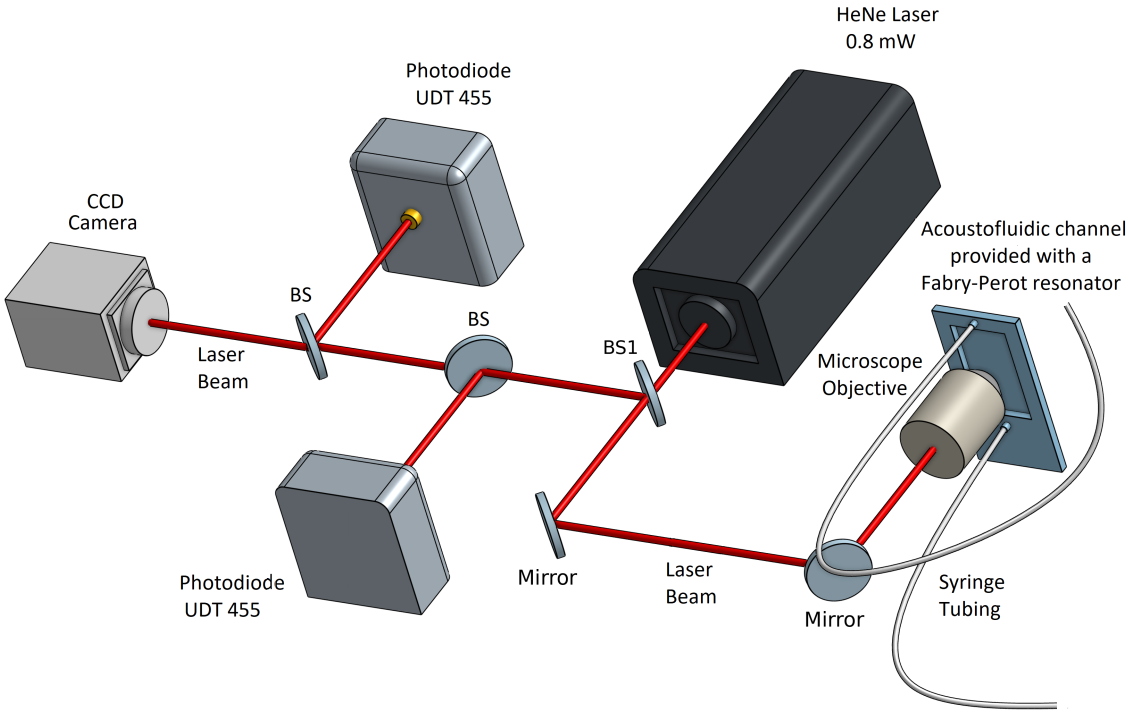

FIGURE 2.4. A He-Ne laser use used as a light source for the microfluidic chip. The laser beam is directed to the microscope objective through beamsplitter BS1 and two steering mirrors and is coupled into the resonator by the microscope objective. The reflected Fabry-Perot fringe pattern is retrieved by the (infinite conjugate) objective and directed, through the same steering mirrors and additional beamsplitters, to the two photodiode detectrs (UDT-455) and to the CCD camera for data analysis.

A BSN10 Thorlabs non-polarizing beamplitter (BS1 – optical Anti-Reflection coating: 400-700 nm), Fig. (2.4), is used in combination with the microscope objective to couple light into the acoustofluidic channel and to retrieve the fringe pattern with the perturbation caused by the cell. The laser beam carrying the RFP is directed to the CCD: an acA1600-20gm Basler camera with a 12-bit resolution. The RFP carrying laser beam is split into two more branches (BS in Fig. (2.4)) and directed to the UDT-455 (OSI Optoelectronics) photodiodes.

The diode detectors can be aligned to detect the fringe pattern perturbation in two different points along the cell path inside the microfluidic channel, allowing for cell speed measurement or detecting the perturbation in the same point for redundancy in the RFP measurements. The one-dimensional nature of the time traces acquired with the photodiode detector is suitable for quasi-real-time analysis. At the same time, the 2D camera images are useful for RFP detailed analysis and device calibration.

2.1.4 Data acquisition

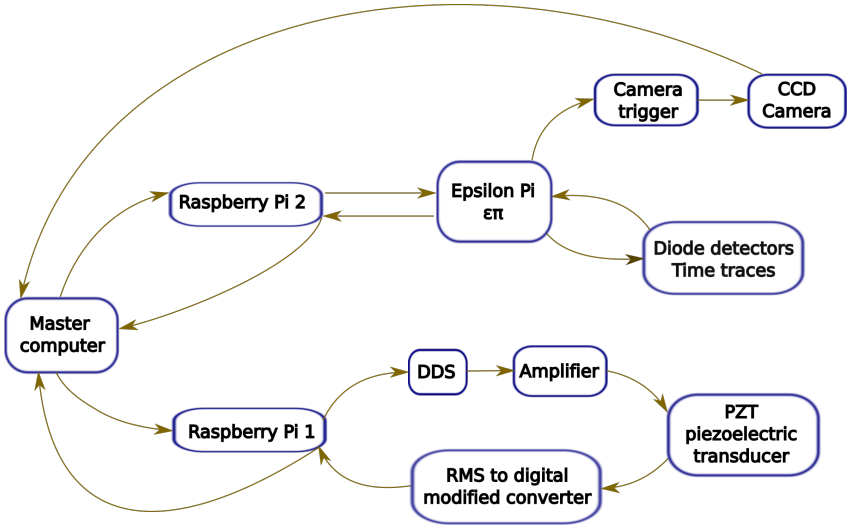

FIGURE 2.5. Flowchart illustrating the chain of electronic elements to coordinate the data acquisition with the acoustofludic interferometric device.

As a first step, the He-Ne laser is turned on to allow for warm-up (its frequency will drift during this time period and the measurements would be unreliable). After warm-up (approximately 15 min) the alignment is optimized for the coupling of the laser into the Fabry-Perot. This is a prototype composed by standard optomechanical components; thus, periodic alignment checks are needed. A computer-controlled procedure precisely identifies the acoustic resonance frequency of the fundamental mode (cf. section 2.1.2). The procedure is performed under the control of the Raspberry Pi Module 1, interfaced with the master computer through an SSH protocol. The raspberry controls the DDS to sweep the frequencies between 6 and 7 MHz in steps of 1 kHz. Simultaneously, the amplitude response at each frequency is measured by conversion through an analog Root Mean Square (RMS) to digital converter (cf. lower branch in the flowchart – Fig. (2.5)). Tuning of the resonance frequency is indispensable as it can vary from day to day due to thermal drifts and differences in fluid density. Once the chip's resonance frequency is identified, the driving amplitude is set to 15 V_{pp} to produce a standing acoustic wave in the water-filled microfluidic channel.

The procedure for image and time trace acquisition, with the flow of acoustically focussed cells, is the following: using the master computer to control the Raspberry Pi2, that drives the Epsilon Pi board (purpose-built for this experiment by ElbaTech Srl) the camera trigger is set to 10 fps and the time-trace acquisition is synchronized with the camera trigger. The photodiodes signal is digitized by the Epsilon Pi and sent to the master computer, as shown in the upper branch of the flowchart in Fig. (2.5). The master computer and the Raspberry Pi 2 are interfaced through the Epsilon PI ZMQ communication layer, allowing for a user interface in which the time trace can be displayed and control all the Epsilon Pi parameters. Acquired time traces and images are sent to the master computer for quasi-real-time analysis or storage.

Data acquisition timing for the time traces is regulated by a Timer period (TIM2PER) and by a Timer multiplier (T2MULT) in the Epsilon Pi module. Data is collected every (TIM2PER × T2MULT) microsecond. The default values of these parameters are: TIM2PER = 100μs and T2MULT = 10, data collection is every 1 ms. The user can change these values by issuing the following commands: SET_TIM2PER (parameter in microseconds) and SET_T2MULT (a conversion factor integer). In the time-traces provided by EpsilonPI ZMQ, the plot X-axis is the number of points in the numeric "Plot points" on the graphic user interface (GUI) (cf. Fig. (2.6)). Parameters can be easily converted to time as: X_time_period_displayed = plot_points × TIM2PER × T2MULT (blue and green framed commands in Fig. (2.6)). The suitable values for our experiment are T2MULT = 1 to get 10 kilo samples per second and set "Plot points"= 10000 to have a plot window period of 1s. It is important to notice that the Y-axis is the sample value at 12bit resolution in the plot. Meaning that 0 is equal to 0 Volt in input, while 4095 is the MAX allowed voltage in the input. Two MAX voltages can be manually selected in the Epsilon Pi board, 500mV or 10V. Our experiments were carried out with a maximum voltage of 500 mV.

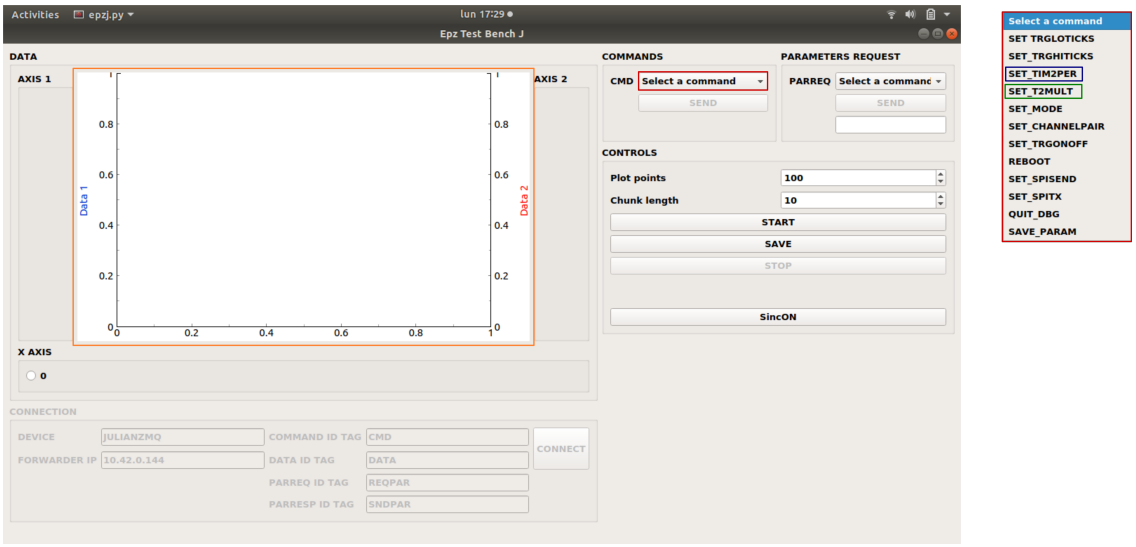

FIGURE 2.6. Screenshot of the EpsilonPI ZQM user interface. The time traces plot display zone is bound in orange. The command menu to control the Epsilon Pi board is bound in red. The timer period command TIM2PER is bound in blue, while the timer multiplier T2MULT is framed in green.

Cell samples

The cell flow is induced with the hydrostatic syringe system to reach a cell sample speed of ≈ 60μm/s. The samples, used one at a time, are:

- Fresh batches of dry, food quality yeast *saccharomyces cerevisiae* hydrated 30 min before each experiment using 40 ml of distilled water and 1 g of yeast.

- 40 ml of a solution of algae *tetraselmis* 6×10^6/ml obtained as a gift from Dr. Chiara Gambardella ISMAR-CNR; the algae were fixed with 2 ml of Lugol. Samples were kept refrigerated at 4 °C.
- 1 ml of standardized microgel beads in a 1×10^6/ml phosphate-buffered saline (PBS) solution for RT-DC [36], obtained from Dr. Salvatore Girardo's team (Max-Planck-Institute for the Science of Light). The sample was diluted with 3 ml of PBS and kept refrigerated at 4 °C. This sample is mono-disperse with a diameter of 15 μm and Young's modulus of 1.7 kPa.
- 3 μm, 8%, variance (highly mono-disperse) polystyrene beads, purchased from Polysciences co. 0.5 ml of the original solution, 1.68×10^9/ml, were diluted in 40 ml of distilled water. Samples were kept refrigerated at 4 °C.

2.2 Gaussian beam behavior inside a Fabry-Perot interferometer

After examining the acoustofluidic operation, we now review the Fabry-Perot theory from an experimental perspective; this allows us to characterize the device and understand its functioning better. In this section, we first analyze the propagation of a Gaussian beam in a Fabry-Perot resonator with particular emphasis on the effect of the beam divergence over Finesse and spot size. The spot size size is relevant since it defines the region where a strong perturbation of the resonator's fringe pattern is observed: the central point of our analysis.

2.2.1 Influence of beam divergence over FP resonator Finesse

In free space, the electromagnetic fields are governed by the so-called Helmholtz equation [11]:

$$\left[\nabla^2 + k^2\right] E(x,y,z) = 0, \tag{2.4}$$

$E(x,y,z)$ is a phasor representing the amplitude of the electric field component and k the wavenumber. Aligning the propagation direction with the z axis, the electric field can be rewritten as:

$$E(x,y,z) = \psi(x,y,z)e^{-ikz}, \tag{2.5}$$

where $\psi(x,y,z)$ describes the evolution of the beam's transverse profile during propagation. Substituting 2.5 into 2.4 we get:

$$\left[\nabla^2\psi - 2ik\frac{\partial\psi}{\partial z}\right] e^{-ikz} = 0. \tag{2.6}$$

In the paraxial approximation (small variations in the field distribution on the wavelength scale):

$$\left|\frac{\partial^2\psi}{\partial z^2}\right| << 2k\left|\frac{\partial\psi}{\partial z}\right|,$$

while the slow variation of propagation on the scale of the transverse extent of the wave implies that

$$\left|\frac{\partial^2\psi}{\partial z^2}\right| << \left|\frac{\partial^2\psi}{\partial x^2}\right|, \left|\frac{\partial^2\psi}{\partial y^2}\right|.$$

By neglecting those terms in eq. (2.6) the paraxial equation is obtained:

$$\frac{\partial^2\psi}{\partial x^2} + \frac{\partial^2\psi}{\partial y^2} - 2ik\frac{\partial\psi}{\partial z} = 0, \tag{2.7}$$

which can be rewritten as

$$\left[\nabla_T^2 - 2ik\frac{\partial}{\partial z}\right]\psi(x,y,z) = 0\,, \tag{2.8}$$

where $\nabla_T^2 = \partial^2\psi/\partial x^2 + \partial^2\psi/\partial y^2$ is the transverse laplacian.

Assuming cylindrical symmetry, the paraxial equation takes the form:

$$\left[\frac{1}{r}\frac{\partial}{\partial r}\left(r\frac{\partial}{\partial r}\right) - 2ik\frac{\partial}{\partial z}\right]\psi(x,y,z) = 0\,. \tag{2.9}$$

Using the following Ansatz:

$$\psi \propto \exp\left[-i\left(P(z) + \frac{kr^2}{2q(z)}\right)\right], \tag{2.10}$$

the following form of the paraxial equation is obtained

$$\left[\frac{k^2}{q^2(z)}\left(\frac{dq(z)}{dz} - 1\right)r^2 - 2k\left(\frac{dP(z)}{dz} + \frac{i}{q(z)}\right)\right] = 0. \tag{2.11}$$

Since the equation must hold for any r and every λ, we then obtain two independent conditions:

$$\frac{dq(z)}{dz} = 1\,, \tag{2.12}$$

$$\frac{dP(z)}{dz} + \frac{i}{q(z)} = 0. \tag{2.13}$$

The solution for eq. (2.12) is simply $q(z) = q_0 + z$.This result clearly shows that q(z) must have the dimensions of a length. However, q_0 cannot be real. If q_0 were real, then the expression (2.10) would imply a beam with a phase change increasing with r, but with a constant amplitude in the field, i.e., a beam with infinite energy [93]. Thus, $q_0 = iz_R$ has to be an imaginary number

$$q(z) = z + iz_R\,. \tag{2.14}$$

The equation (2.13) solution is:

$$iP(z) = \ln\left[1 - i\left(\frac{z}{z_R}\right)\right]. \tag{2.15}$$

Taking the exponential of the negative of eq. (2.15) and then combining all the terms, the resulting expression for the electric field becomes:

$$\frac{E(x,y,z)}{E_0} = \frac{1}{\left[1 + (z/z_R)^2\right]^{1/2}}\exp\left[-\frac{kz_R r^2}{2(z^2 + z_R^2)}\right]\exp\left[-i\frac{kzr^2}{2(z^2 + z_R^2)}\right]\exp\left[i\arctan\left(\frac{z}{z_R}\right)\right]\exp(-ikz). \tag{2.16}$$

Introducing the following definitions:

Beam waist:

$$w_0 = \sqrt{\frac{2z_R}{k}}, \tag{2.17}$$

Rayleigh length (eq. (2.14) evaluated at $z = 0$):

$$q(0) = iz_R = i\frac{\pi w_0^2}{\lambda}, \tag{2.18}$$

Spot size:

$$w(z) = w_0\sqrt{1+\left(\frac{z}{z_R}\right)^2}, \tag{2.19}$$

Radius of curvature:

$$R(z) = z\left[1+\left(\frac{z_R}{z}\right)^2\right], \tag{2.20}$$

and the Guoy phase shift:

$$\phi(z) = \arctan\left(\frac{z}{z_R}\right), \tag{2.21}$$

we obtain the final form of the electric field:

$$\frac{E(x,y,z)}{E_0} = \frac{w_0}{w(z)}\exp\left[-\frac{r^2}{w^2(z)}\right]\exp\left[-i\frac{kr^2}{2R(z)}\right]\exp\left[-i\left(kz-\phi(z)\right)\right]. \tag{2.22}$$

Is important to note that the Gaussian beam at the origin $z = 0$ has a planar wavefront and the minimum spot size, also is the point where the spot size has its minimum value.

2.2.1.1 Physical meaning of the Rayleigh length

When $z = z_R$ the expression for the beam radius eq. (2.19) reads:

$$w(z) = w_0\sqrt{1+\left(\frac{z_R}{z_R}\right)^2} = \sqrt{2}w_0\,. \tag{2.23}$$

The size of the beam has expanded $\sqrt{2}$ times, relative to the waist position (origin of the reference system), and a factor 1/e reduces the electric field amplitude.

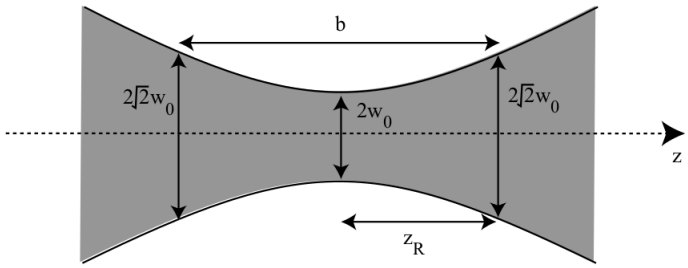

FIGURE 2.7. Gaussian beam schematics. w_0 is the beam waist, z_R is the Rayleigh length, b is the confocal parameter (twice z_R), and the beam spot size at the Rayleigh length is $w(z_R) = \sqrt{2}w_0$.

It is also important to highlight that the radius of curvature of the wavefront is the smallest at the Rayleigh length. From the beam waist, the curvature evolves from planar to strongly curved (radius of curvature equal to the confocal parameter) and then to the one of the spherical wave, centered on the beam waist a large distance.

2.2.1.2 Beam Divergence

When $z >> z_R$ eq. (2.19) becomes

$$w(z) = w_0\sqrt{1+\left(\frac{z}{z_R}\right)} \simeq w_0\left(\frac{z}{z_R}\right),$$

a linear function of z. We can therefore introduce the beam divergence θ , costant when $z \gg z_R$:

$$\frac{w}{z} = \frac{w_0}{z_R} = \frac{\lambda}{\pi w_0} = \tan(\theta) \simeq \theta\,, \tag{2.24}$$

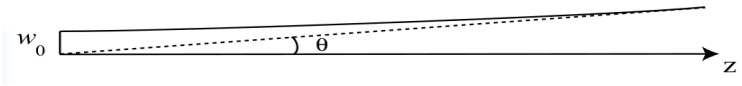

FIGURE 2.8. The angle of divergence of a Gaussian beam, the divergence is measured from the beam waist.

2.2.1.3 Beam spreading in a Fabry-Perot resonator

Light traveling in roundtrips inside an optical resonator (assuming ideal mirrors of 100 % reflectivity) is physically equivalent to light propagation in free space over a distance $L \cdot \mathscr{F}$ where ℓ is the mirror's separation and $\mathscr{F}$ the Finesse. The Finesse can be interpreted as the number of roundtrips that one photon will travel before exiting the resonator. The beam will continue diverging and after several roundtrips (like traveling in free space) and the beam radius will increase due to the Gaussian beam divergence inside the resonator (cf. Fig. (2.8)).

Discussing such divergence is important since the spreading of the beam inside the resonator will eventually reduce the Finesse of the Fabry-Perot cavity due to the interference between roundtrips where the beam diameter is not constant. Consequently, only those photons that belong to the surface common to all beams are going to interfere (using an intuitive picture), thereby reducing the fringe contrast due to the decreased electromagnetic field amplitude of the larger beam. In the end, this effect reduces the Finesse of the interferometer.

2.2.2 Gaussian beam focused by a thin lens

If we want to consider a Gaussian beam with a thin lens, we need to know the object's beam waist size and position. Once this is known, we can easily find the image beam waist size (equivalent to the focussed spot in geometrical optics, but with a finite size) and its position. Figure 2.9 illustrates the definitions, where subscript 1 refers to the object beam and 2 to the imaged beam.

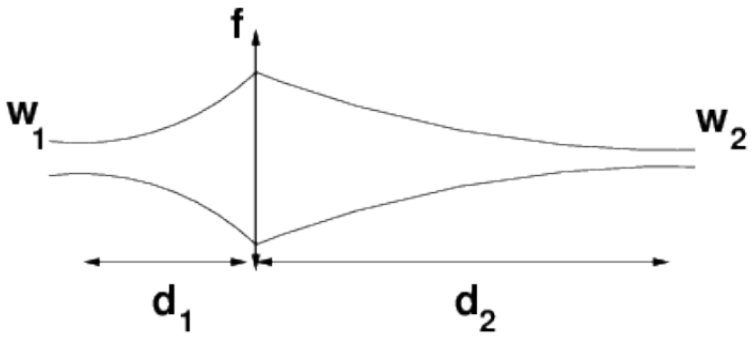

FIGURE 2.9. Change of the beam waist of a Gaussian beam focussed by a thin lens. The subscript 1 refers to the object and 2 to the image.

The transformations are given by [93]:

$$w_2^2 = w_1^2 \frac{f^2}{(d_1-f)^2+z_{R,1}^2}, \tag{2.25}$$

$$d_2 = f+(d_1-f)\frac{f^2}{(d_1-f)^2+z_{R,1}^2}, \tag{2.26}$$

where $z_{R,1}$ is the Rayleigh length of the incoming beam (2.18).

The microscope objective used in our experiment (Olympus 20X, Plan Achromatic) is conjugated to infinity and has a specified focal length $f_o = 9$ mm, with working distance $d_w = 1.2$ mm. This means that the exit focal plane is well inside the housing (from the numbers, it is placed 7.8 mm back from the front housing). Thus, in a geometrical optics approximation, we can assume that a spherical wave with a radius of curvature $R = 9$ mm exits the housing to reach its focus 1.2 mm after the front of the objective. For the laser, Thorlabs HNLS008L-EC, the waist size is specified as the $\frac{1}{e^2}$ point of the *intensity*. Since eqs. (2.25-2.26) require the $\frac{1}{e}$ *radius* of the field; we need to transform the value specified by the manufacturer.

2.2.2.1 $1/e^2$ beam diameter conversion to beam waist

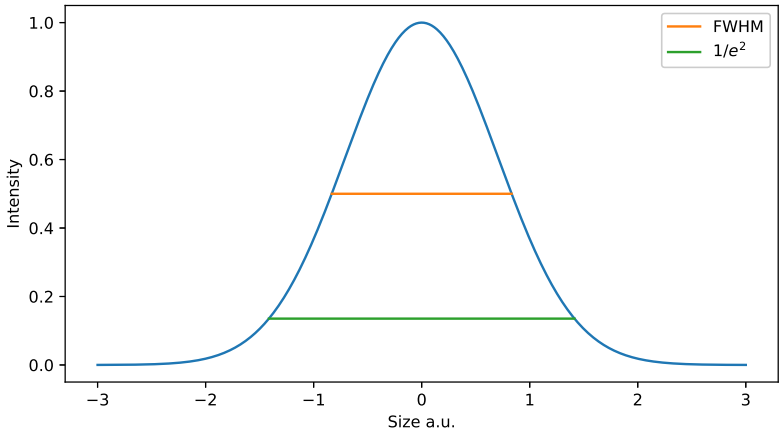

FIGURE 2.10. Different experimental parameters to characterize a Gaussian beam diameter.

To keep the calculation as simple as possible, we consider the transverse Gaussian envelope (blue line in Fig. (2.10)) and write it in the simplified form

$$E(\rho) \propto e^{-\frac{\rho^2}{r^2}} \tag{2.27}$$

where $E(\rho)$ represents the electric field envelope's dependence on the radial coordinate ρ and r stands for the beam radius.

Passing to the beam intensity

$$I(\rho) \propto E^2(\rho), \tag{2.28}$$

$$\propto e^{-2\frac{\rho^2}{r^2}}, \tag{2.29}$$

$$= e^{-\frac{\rho^2}{r_I^2}}, \tag{2.30}$$

where we have denoted with r_I the radius for the intensity distribution, which is – in this form – automatically defined at the $\frac{1}{e^2}$ point. Notice that $r_I^2 = \frac{r^2}{2}$.

We then introduce the diameter for the intensity at the same level $d_I = \frac{I(0)}{e^2}$

$$d_I = 2r_I, \tag{2.31}$$

and with the following simple identifications, we arrive at a relationship between the intensity diameter d_I and the field radius r:

$$d_I = 2r_I, \tag{2.32}$$
$$= 2\frac{r}{\sqrt{2}}, \tag{2.33}$$
$$r = \frac{\sqrt{2}}{2}d_I. \tag{2.34}$$

From the Thorlabs laser specifications

$$d_I = 0.48mm, \tag{2.35}$$
$$w_1 \equiv r = 0.34mm. \tag{2.36}$$

Notice that the field radius matches the beam waist in Fig. (2.7), and is related to the beam diameter at $1/e^2$ shown in Fig.(2.10) by the fact that the first is a longitudinal cut of the Gaussian beam electric field. In contrast, the second represents the intensity of the electric field in a transversal cut.

The beam waist position is not specified, but customarily He-Ne lasers are built with a planar output coupler. We can therefore safely assume that the beam waist is placed at the laser exit (planar wavefront) and, considering a distance $d_1 \approx 0.3$ m (accordingly to our experimental setup), we obtain for a lens with focal distance $f = 0.009$ m (an equivalent thin lens for the microscope objective placed at d_1)

$$w_2 \approx 4.76 \times 10^{-6}\,\mathrm{m}, \tag{2.37}$$
$$d_2 = 0.009057\,\mathrm{m}, \tag{2.38}$$

computed for a Rayleigh length (cf. eq. (2.18))

$$z_{R,1} = \frac{\pi w_1^2}{\lambda}, \tag{2.39}$$
$$= 0.574\mathrm{m}, \tag{2.40}$$

where we have equated the computed value of the radius r to the beam waist size w_0.

Thus, the imaged beam waist is approximately 4.8μ m and is placed 0.06 mm beyond the focal plane of the microscope objective. The difference is tiny, even though it represents 1/3 of the coverslip thickness, which constitutes the Fabry-Perot's front mirror.

2.3 Influence of Fabry-Perot's mirror distance

Two different experimental configurations for cytometry can be distinguished on the basis of the ratio between the Fabry-Perot resonator length L and cell diameter ℓ. The difference between the two arrangements is not restricted to the pure requirements of the setup, but is based on the interferometer's response, as in one case one expects a shift in the fringe pattern, in the other one to a fringe modification. If $L \approx 2\ell$ (cf. Fig. (2.11), matching a small-gap interferometer), the main effect of observing will be a shift in the Airy's transmission function [95]. On the contrary, if $L \gg \ell$ the observed phenomenon will be a thin lens-like perturbation in the RFP.

It is important to highlight that a high Finesse is required for a small-gap Fabry-Perot resonator, as the fringe shift needs to be accurately measured. This requires a combined reflectance for the two mirrors $R \gtrsim 0.7$. In contrast, the large-gap FP resonator, as the one we use, where $L \gtrsim 10 \times \ell$, operates at its best in a low-Finesse configuration and can operate with a combined reflectivity $R \approx 0.04$, successfully detecting a cell inside the interferometer. It is important to realize that a very high Finesse would render the task more difficult in large-gap resonators as the perturbation induced by the cell would amount to a shift of several fringes instead of the displacement of a single one characteristic of the small-gap configuration. The multiple fringe shift would increase the probability of miscounting one fringe, thus leading to measurement errors.

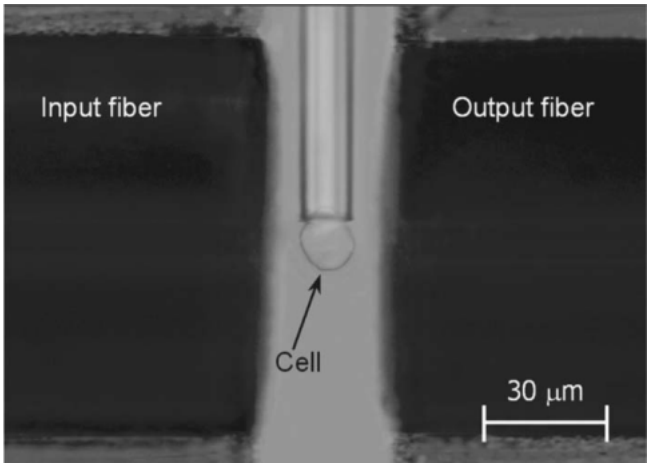

FIGURE 2.11. A Fabry-Perot resonator was created by using two fiber optic ends. The separation between the semi-reflective surfaces is approximate twice the cell size. Figure taken from [95].

2.3.1 Cell phase shift in a small-gap FP resonator

From eq. (1.1), the difference in the optical path caused by the reflection of the light into a layer (or the etalon of the Fabry Pérot interferometer) at normal incidence is:

$$\delta = 2nkL\,, \tag{2.41}$$

where n is the medium's refractive index, k is the wavenumber and ℓ the physical length.

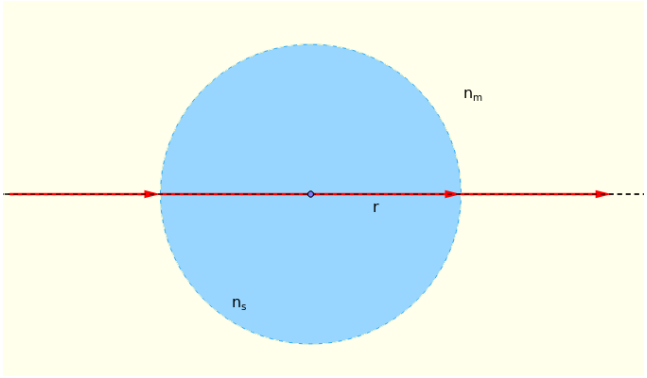

Figure 2.12: Beam propagating through the diameter of a sphere.

As a first approximation, we can consider the cell as a sphere placed at the center of a Fabry-Perot resonator. The new optical path difference will be the contribution of the FP etalon and that of the cell's optical path Fig. (2.12). Using the superposition principle:

$$\delta = 2n_m L + 2(n_s - n_m)(2r), \tag{2.42}$$

for a ray passing through the center of the sphere and aligned with the resonator axis (cf. Fig. (2.12)). The meaning of the symbols in eq. (2.42) is: n_m and n_s refractive index of medium and sphere, respectively, ℓ distance between the Fabry-Perot mirrors and r sphere radius. Because of the intrinsic convergence (or divergence) of the Gaussian beam issued by the laser, we must also consider non-normal incidence onto the sphere. This can be achieved with the help of Fig. (2.13), and amounts to the following phase shift

$$\delta = 2n_m L + 2(n_s - n_m)(2r\cos(\alpha)) \tag{2.43}$$

where α is the angle depicted in the figure (2.13).

Besides, as the sphere enters and exits the interferometer's spot size (as described in sect. 2.1), the incidence is no longer normal even for a plane wave. Thus there is a progressive change in path difference which reduces to the one of the empty interferometer as $\alpha \to 0$.

$\alpha = 0$ represents light propagating through the sphere's center while increasing values of α match the situation where the light passes through a cord parallel to the diameter of a sphere that moves out of the beam spot. The value of $\alpha = 90°$ represents the absence of the sphere in the resonator's beam spot.

This is only a toy model of the real effect of the sphere on the optical path difference since, as we can see from Fig. (2.13) , the beam will undergo different refraction angles depending on the distance b at which it traverses the sphere.

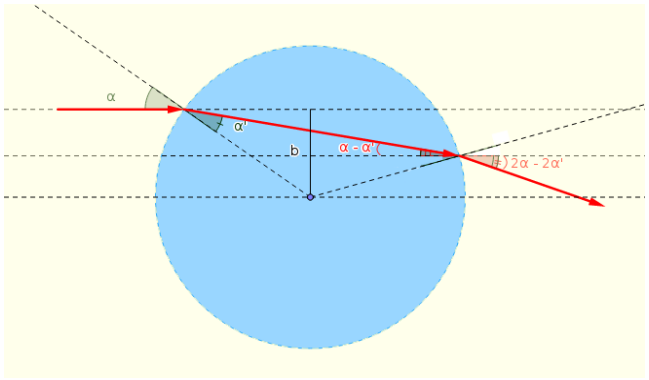

FIGURE 2.13. Beam propagating through a sphere at a distance b from the center. n_s, r are the sphere's refractive index and radius, respectively. A beam having an angle of incidence $\alpha = \arcsin(b/r)$ will be refracted by the sphere at an angle $2\alpha - 2\alpha'$, where $\alpha' = \arcsin(b/rn_s)$.

2.3.1.1 Airy's function modification

The transmittance of Airy's function for the Fabry-Perot interferometer according with the eq. (1.14) is:

$$T = \frac{1}{1 + F\sin^2(\delta/2)}, \tag{2.44}$$

where F is the coefficient of finesse, eq. (1.11). Using the expression for the phase shift δ in the presence of the cell, the FP transmission function becomes:

$$T = \frac{1}{1 + F\sin^2\left(\left(\frac{2\pi}{\lambda}\right)[n_m l + (n_s - n_m)r\cos(\alpha)]\right)}, \tag{2.45}$$

or, in terms of the reflected intensity and following eq. (1.15), the reflection function reads:

$$R = \frac{1}{1 + \frac{1}{F}\csc^2\left(\left(\frac{2\pi}{\lambda}\right)[n_m l + (n_s - n_m)r\cos(\alpha)]\right)}. \tag{2.46}$$

2.3.1.2 The resolution power of the small-gap FP interferometer

The immersion of the cell inside the FP interferometer, Fig. (2.11), changes the total optical path difference, which now has two components: one provided by the light traversing the cell and the second corresponding to the etalon thickness minus the cell diameter. Thus the resonance condition of the FP resonator eq. (1.16) in its form, $2nL = m\lambda$ becomes, with the help of eq. (2.42):

$$2n_m L + 2(n_c - n_m)\ell = m\lambda \tag{2.47}$$

where L is the mirror separation, $\ell = 2r$ is the cell diameter, n_m and n_c are the refractive indices of medium and cell, respectively.

Exploiting the cell's deformability as a label-free biomarker is one of the main goals of our work. Thus, the acoustofluidic interferometric device's sensitivity to the acoustically-induced changes in cell diameter ℓ is an important feature. From eq. (2.47) we can see that the diameter of the cell ℓ is a linear function of the order m,

$$\ell = \frac{\lambda}{2(n_c - n_m)} m - \frac{n_m}{n_c - n_m} L. \tag{2.48}$$

The complete size reconstruction is problematic since it depends on an exact knowledge of m (not a trivial task in interferometry) and of n_c. In addition, one has to have very good control of ℓ, as well. However, the diameter's rate of change can be analyzed as follows:

$$\frac{\Delta\ell}{\Delta m} = \frac{\lambda}{2(n_c - n_m)}. \tag{2.49}$$

Since the Finesse is related to the FSR-FWHM ratio of the individual fringes (see eq. (1.23)) and given that a change in the order $m \to m+1$ implies a phase change of π, is possible to assign to the quantity

$$\text{Resolution} = \frac{\Delta\ell_1}{\Delta m} \frac{1}{\mathscr{F}} \tag{2.50}$$

the role of minimal resonator resolution (cf. Fig. (2.14)). This expression is valid under the assumption the phase change comes exclusively from the change in cell size. If we consider a resonator with Finesse 10, this will imply that the FWHM fits 10 times in the FSR. Supposing a cell of l =100 μm diameter and a phase change of π – corresponding to a 10% change in the cell diameter ℓ – then the interferometer's minimal resolution will be $1\,\mu m$.

Reflectivity	Coefficient of finesse	Finesse	Resolution [μm]
0.3	2.45	2.46	4.28
0.9	89.75	14.88	0.7
0.99	9898.73	156.28	0.07

TABLE 2.1. Different values of reflectivity, Finesse, coefficient of finesse and resolution of a small-gap Fabry-Perot resonator. The expressions for the coefficient of finesse, Finesse, and resolution are given by eqs. eq. (1.11), eq. (1.19) and eq. (2.50), respectively. A change in the cell diameter of $\Delta\ell$ =10 μm was assumed for the calculation of the resolution.

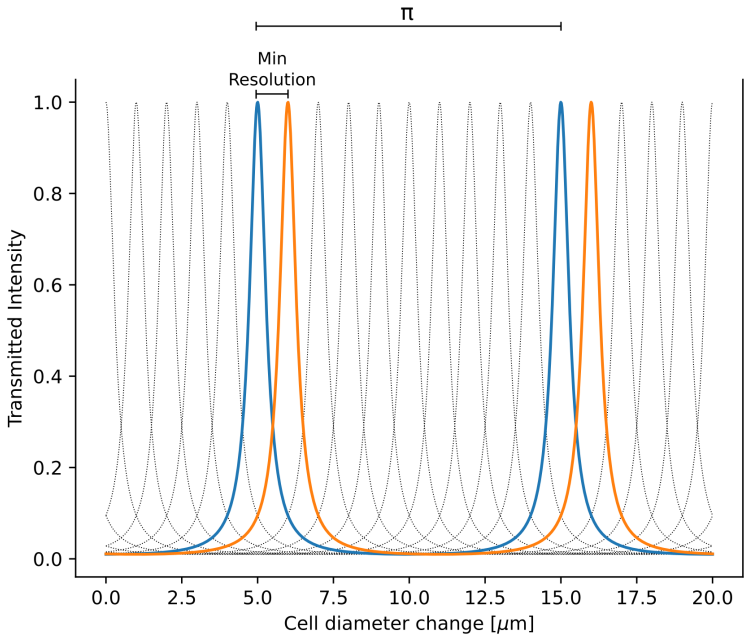

FIGURE 2.14. The Airy's transmission function of a small-gap Fabry-Perot resonator with a cell of 100 μm inside. A Finesse of $\mathscr{F} = 10$ is plotted in blue. The change in phase caused by a cell's change diameter of 1 μm is plotted in orange. The phase change between the two blue maxima is π and given that the $\mathscr{F} = 10$. 10 dotted maxima fit between the two blue maxima.

2.4 Low Finesse Fabry-Perot resonator

The low-Finesse configuration provided by the large-gap Fabry-Perot interferometer has been chosen due to its high throughput potential in optomechanical properties-based cytometry. The low-Finesse configuration has better flexibility for the integration of the cells' acoustic manipulation. The high-Finesse configuration is based on a cell holder to position the cell inside the resonant cavity; such a system is indeed incompatible with the high throughput (cf. Fig. (2.11)) and the acoustic focusing implementation is not easy. In addition, a fringe shift measurement requires high stability at the interferometric level, which requires, on the one hand, continuous calibration (e.g., for changes in pressure inside the microfluidic channel), but also an excellent overall stability of the whole support.

2.4.1 Spherical wavefront interference in a large-gap Fabry Perot configuration

The device developed comprises a Fabry-Perot interferometer where the channel width, which serves as the mirror separation ℓ, is much larger than the cell diameter: $L \gtrsim 10 \times \ell$. A long channel is needed for acoustic excitation. The fundamental resonance of the channel would become too high for excitation through piezoelectric transducers available in reasonable sizes and costs. As was shown in the previous subsections, this experimental configuration allows for observing the change in the RFP caused by the cell, rather than a simple phase shift which results from the small-gap ($L \approx \ell$) Fabry-Perot resonator.

This subsection addresses how to study the fringe pattern perturbation induced by a cell, modeled as a thin lens, in this resonator configuration. First, a ray-matrix approach is used to model the propagation of the light in the low-Finesse Fabry Perot resonator containing a thin lens (cell proxy). Next, the radius of curvature of the reflected wave is computed to retrieve the Cell Focal Length (CFL).

Fig. (2.15) illustrates the interferometer (cf. caption for details) and assumes that the incident laser beam is focused onto the front face of the glass plate (the definition is generic, thus any other point can be chosen).

Taking into account the refractive index of each medium, the optical path, denoted by a tilde over the corresponding symbol, becomes

$$\tilde{L} = n_w L, \tag{2.51}$$

$$\tilde{t}_c = n_g t_c, \tag{2.52}$$

$$\tilde{t}_m = n_g t_m \tag{2.53}$$

where n_w and n_g are the water and glass refractive indices, respectively, and

$$\mathscr{L}_1 = \tilde{t}_c + \frac{1}{2}\tilde{L}, \tag{2.54}$$

$$\mathscr{L}_2 = \tilde{L} + 2\tilde{t}_m, \tag{2.55}$$

are the optical paths measured on either side of the lens. A spherical lens approximates the cell with a radius of curvature r_c and refractive index n_c. Using the thin lens formula, we can obtain its equivalent focal lens

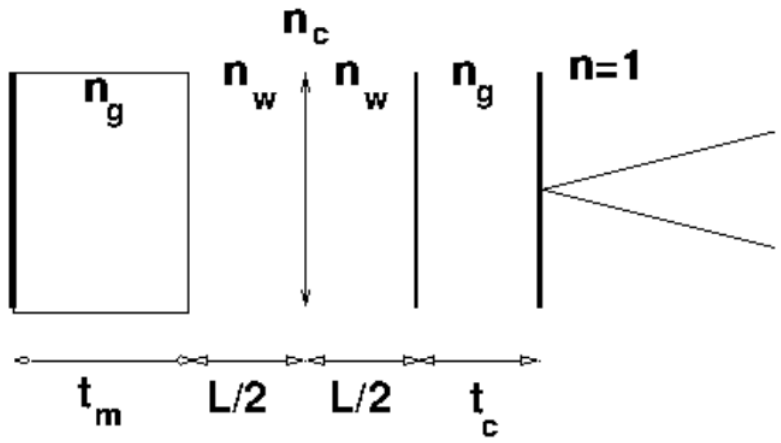

FIGURE 2.15. Schematics of the different interfaces in a low-Finesse Fabry-Perot resonator, analogous to the one used in our AID (cf. section (2.1)). n is the refractive index of air, n_g and n_w those of glass and water, respectively. t_m, ℓ and t_c represent the back mirrors glass substrate's thickness, the water-filled microfluidic channel, and the front glass surface delimiting the channel, respectively.

$$f_c = \frac{r_c}{2(n_c - n_w)}. \tag{2.56}$$

The focal distance is assumed to be very long, $f_c \gg r_c$, justifying the thin lens approximation. In our system, $\frac{f_c}{r_c} = \frac{1}{2(n_c - n_w)} \gg 1$ due to the closeness of the medium's and cell's refractive indices (typically within a few percent). Thus, the focal length is indeed always much larger than the cell radius. Notice, however, that the focal length is not required to be small compared to the resonator's length (and is not even necessarily expected to be so).

The beam evolution inside the resonator can be computed with the beam propagation matrices:

$$\tilde{M} = M_{\mathscr{L}_1} \cdot M_\ell \cdot M_{\mathscr{L}_2} \cdot M_\ell \cdot M_{\mathscr{L}_1}, \tag{2.57}$$

where the expressions for the various matrices are [93]:

$$M_{\mathscr{L}_1} = \begin{pmatrix} 1 & \mathscr{L}_1 \\ 0 & 1 \end{pmatrix}, \tag{2.58}$$

$$M_{\mathscr{L}_2} = \begin{pmatrix} 1 & \mathscr{L}_2 \\ 0 & 1 \end{pmatrix}, \tag{2.59}$$

$$M_\ell = \begin{pmatrix} 1 & 0 \\ -\frac{1}{f_c} & 1 \end{pmatrix}. \tag{2.60}$$

f_c is the cell's focal length defined above, eq. (2.56), $M_{\mathscr{L}_1}$ represents the propagation between the resonator entrance (considered as the interface glass-air, cf. Fig (2.15)) and the thin lens. The thin lens,

represented by M_ℓ, is symmetrically placed inside the acoustic channel and $M_{\mathscr{L}_2}$ is the roundtrip from the thin lens, to the mirror and back to the lens.

At this level of approximation, we are ignoring the reflection at the glass-water interface given that the normal reflection coefficients, computed with

$$r = \left(\frac{n_1 - n_2}{n_1 + n_2}\right)^2, \tag{2.61}$$

where n_1 and n_2 are the two media's refractive indices, are $R_{air-glass} \approx 0.04$ and $R_{glass-water} \approx 0.004$, respectively. Thus, the approximation of neglecting the glass-water interface appears reasonable. This reflectivity value $r_{air-glass} \approx 0.04$ and a reflectivity value of $r_{mirror} = 0.9$ corresponds, for a resonator without a thin lens inside, to a Finesse (eq. (1.19)) of 0.61, whence the denomination "low-Finesse" FP resonator.

Expanding the algebra, we obtain a transfer matrix

$$\tilde{M} = \begin{pmatrix} A & B \\ C & D \end{pmatrix}, \tag{2.62}$$

with coefficients

$$A = \frac{f_c^2 - [\mathscr{L}_2 + 2\mathscr{L}_1] f_c + \mathscr{L}_1\mathscr{L}_2}{f_c^2}, \tag{2.63}$$

$$B = \frac{[\mathscr{L}_2 + 2\mathscr{L}_1] f_c^2 - 2\mathscr{L}_1[\mathscr{L}_2 + \mathscr{L}_1] f_c + \mathscr{L}_1^2\mathscr{L}_2}{f_c^2}, \tag{2.64}$$

$$C = \frac{\mathscr{L}_2 - 2f_c}{f_c^2}, \tag{2.65}$$

$$D = \frac{f_c^2 - [2\mathscr{L}_1 + \mathscr{L}_2] f_c + \mathscr{L}_1\mathscr{L}_2}{f_c^2}, \tag{2.66}$$

Notice that the expression

$$2\mathscr{L}_1 + \mathscr{L}_2 = 2(\tilde{t}_m + \tilde{L} + \tilde{t}_c), \tag{2.67}$$

corresponds to one full roundtrip (optical length) inside the resonator.

We have ignored the multiple reflections inside the Fabry-Perot resonator and have considered just one roundtrip in this procedure. The reason for considering, at least in the first approximation, only the first roundtrip and not the multiple interferences inside the resonator is the ratio between the intensities of the various waves. The first glass-air interface transmits approximately $0.96 I_{in}$ (I represent the Poynting vector of each component). Accounting for the finite reflectivity of the back-mirror R_b and for the losses at the glass-water interface, we find that the intensity exiting the resonator after the first roundtrip is $\approx 0.91 R_b I_{in}$, while the component reflected back into the resonator after the first roundtrip will be $0.04 \times 0.95 R_b I_{in} \approx 0.038 R_b I_{in}$. Thus only $\approx 3.8\%$ of the intensity goes for a second roundtrip and we thus neglect this component in our low-Finesse Fabry-Perot resonator.

From [93], the radius of curvature R_{out} of the wavefront exiting the resonator after one roundtrip, as a function of the entering wavefront curvature, is

$$R_{out} = \frac{A \cdot R_{in} + B}{C \cdot R_{in} + D}, \tag{2.68}$$

thus, the two wavefronts R_{in} (reflected by the back mirror) and R_{out} exiting the resonator, can be superposed to compute their circular interference fringes (cf. Fig. (2.16)).

2.4.1.1 Computing Fabry-Perot interference rings

Fig. (2.16), describes the geometric construction used to identify the values of the distance from the optical axis, ρ, where constructive interference fringes (bright rings) are expected.

The positions of the two origins for the two emerging waves is arbitrary (the two could be exchanged). The problem is solved in cylindrical coordinates. Thus the azimuthal angle ϕ is neglected. The distance from the axis is ρ (cf. Fig. (2.16)).

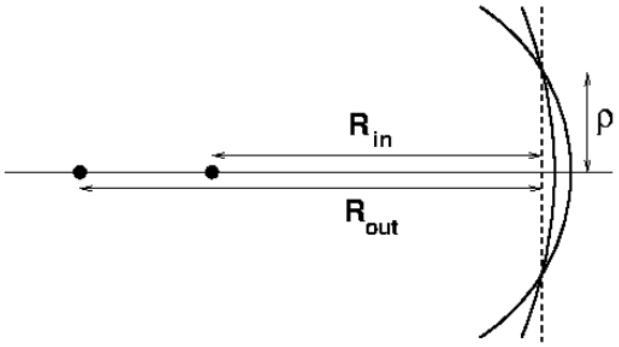

FIGURE 2.16. Schematics of the exiting (R_{out}) and retroreflected (R_{in}) wavefronts were interfering at the plane of the microscope objective. The respective origins for the two curved wavefronts match the radii of curvature. The relative positions are arbitrarily marked, as the value of R_{out}, relative to R_{in}, depends on experimental parameters. ρ is the coordinate measuring distances from the optical axis.

We define the distance from the axis ρ_1 as the one for which we find the first bright fringe:

$$\sqrt{R_{out}^2 + \rho_1^2} - \sqrt{R_{in}^2 + \rho_1^2} = m\lambda, \tag{2.69}$$

where we define the integer m such that [9]

$$R_{out} = R_{in} + (m-1)\lambda + \epsilon, \tag{2.70}$$

$$0 \leq \epsilon < \lambda, \tag{2.71}$$

$$m = 1 + Int\left[\frac{R_{out} - R_{in}}{\lambda}\right]. \tag{2.72}$$

Solving for R_{out} for two consecutive bright fringes ρ_1 and ρ_2 (eq. (2.69)):

$$\sqrt{R_{out}^2+\rho_1^2}-\sqrt{R_{in}^2+\rho_1^2} = m\lambda \tag{2.73}$$

$$\sqrt{R_{out}^2+\rho_2^2}-\sqrt{R_{in}^2+\rho_2^2} = (m+1)\lambda, \tag{2.74}$$

we obtain

$$R_{out} = \pm\sqrt{\frac{1}{4k^2}\left[\rho_2^2-\rho_1^2-k^2\right]^2-\rho_1^2}, \tag{2.75}$$

$$k = \lambda+\sqrt{R_{in}^2+\rho_2^2}-\sqrt{R_{in}^2+\rho_1^2}, \tag{2.76}$$

2.4.1.2 Cell focal length (CFL) computation

Substituting eqs. (2.63) – (2.66) into eq. (2.68), we can obtain a quadratic equation for f_c (eq. (2.77)), which is the quantity that we want to obtain experimentally,

$$d_2 f_c^2+d_1 f_c+d_0 = 0, \tag{2.77}$$

$$d_2 = (R_{in}-R_{out})+[\mathscr{L}_2+2\mathscr{L}_1], \tag{2.78}$$

$$d_1 = 2R_{in}R_{out}+(R_{out}-R_{in})[\mathscr{L}_2+2\mathscr{L}_1]-2\mathscr{L}_1[\mathscr{L}_2+\mathscr{L}_1], \tag{2.79}$$

$$d_0 = (R_{in}-R_{out}+\mathscr{L}_1)\mathscr{L}_2\mathscr{L}_1-R_{in}R_{out}\mathscr{L}_2. \tag{2.80}$$

The cell focal length (CFL) f_c is determined by computing the two roots of the second degree algebraic equation (2.77):

$$f_c+ = \frac{-d_1+\sqrt{d_1^2-4d_2d_0}}{2d_2} \tag{2.81}$$

$$f_c- = \frac{-d_1-\sqrt{d_1^2-4d_2d_0}}{2d_2} \tag{2.82}$$

The cell radius, connected to the focal length of the associated thin lens, is obtained by inverting eq. (2.56), once the cell refractive index is known:

$$r_c = 2(n_c-n_w)f_c. \tag{2.83}$$

2.4.2 Uncertainty analysis

To get an idea of the sensitivity of the measurement and the expected uncertainties, we perform an analysis of the experimental procedure.

The examination is separated into two parts:

1. Sensitivity and uncertainty on the output radius of curvature obtained from the interferometric fringes;

2. Sensitivity and uncertainty on the estimated focal length induced by the (sperical) object.

2.4.2.1 Output radius of curvature

Starting from the expression relating the measured interference fringes to the two radii of curvature eq. (2.75)

$$R_{out} = \pm\sqrt{\frac{1}{4k^2}\left[\rho_2^2-\rho_1^2-k^2\right]^2-\rho_1^2}, \tag{2.84}$$

$$k = \lambda+\sqrt{R_{in}^2+\rho_2^2}-\sqrt{R_{in}^2+\rho_1^2}, \tag{2.85}$$

with ρ_1 and ρ_2 the first two interference fringes starting from the center of the pattern, and λ laser's wavelength.

We need to compute all derivatives with respect to the variables. Given the complexity of the expressions, we can use the chain rule for the derivatives and start by calculating those for k

$$\frac{\partial k}{\partial R_{in}} = R_{in}\left(\frac{1}{\sqrt{R_{in}^2+\rho_2^2}}-\frac{1}{\sqrt{R_{in}^2+\rho_1^2}}\right), \tag{2.86}$$

$$\frac{\partial k}{\partial \rho_1} = -\frac{\rho_1}{\sqrt{R_{in}^2+\rho_1^2}}, \tag{2.87}$$

$$\frac{\partial k}{\partial \rho_2} = \frac{\rho_2}{\sqrt{R_{in}^2+\rho_2^2}}, \tag{2.88}$$

where we neglect the sensitivity with respect to wavelength since we consider it a fixed quantity (He-Ne laser) since the wavelength is very stable and known with at least four digits.

With the help of the previous expressions, we can compute the sensitivity of R_{out}

$$\frac{\partial R_{out}}{\partial R_{in}} = \frac{\partial R_{out}}{\partial k}\frac{\partial k}{\partial R_{in}}, \tag{2.89}$$

$$\frac{\partial R_{out}}{\partial k} = \pm\frac{1}{2}\frac{-\frac{1}{2k^3}\left[\rho_2^2-\rho_1^2-k^2\right]^2-\frac{1}{k}\left[\rho_2^2-\rho_1^2-k^2\right]}{\sqrt{\frac{1}{4k^2}\left[\rho_2^2-\rho_1^2-k^2\right]^2-\rho_1^2}}, \tag{2.90}$$

$$\frac{\partial R_{out}}{\partial \rho_1} = \frac{\partial R_{out}}{\partial k}\frac{\partial k}{\partial \rho_1}+\frac{\partial R_{out}}{\partial \rho_1}, \tag{2.91}$$

$$\frac{\partial R_{out}}{\partial \rho_2} = \frac{\partial R_{out}}{\partial k}\frac{\partial k}{\partial \rho_2}+\frac{\partial R_{out}}{\partial \rho_2}, \tag{2.92}$$

$$\frac{\partial R_{out}}{\partial \rho_1} = \pm\frac{1}{2}\frac{-\frac{\rho_1}{k^2}\left[\rho_2^2-\rho_1^2-k^2\right]-2\rho_1}{\sqrt{\frac{1}{4k^2}\left[\rho_2^2-\rho_1^2-k^2\right]^2-\rho_1^2}}, \tag{2.93}$$

$$\frac{\partial R_{out}}{\partial \rho_2} = \pm\frac{1}{2}\frac{\frac{\rho_2}{k^2}\left[\rho_2^2-\rho_1^2-k^2\right]}{\sqrt{\frac{1}{4k^2}\left[\rho_2^2-\rho_1^2-k^2\right]^2-\rho_1^2}}., \tag{2.94}$$

From the quadratic propagation of uncertainties, we can obtain the expected error on the output radius of curvature, as a function of all other uncertainties:

$$\Delta R_{out} = \sqrt{\left(\frac{\partial R_{out}}{\partial R_{in}}\right)^2 \Delta R_{in}^2 + \left(\frac{\partial R_{out}}{\partial \rho_1}\right)^2 \Delta \rho_1^2 + \left(\frac{\partial R_{out}}{\partial \rho_2}\right)^2 \Delta \rho_2^2}, \tag{2.95}$$

$$= \sqrt{\left(\frac{\partial R_{out}}{\partial k}\frac{\partial k}{\partial R_{in}}\right)^2 \Delta R_{in}^2 + \left(\frac{\partial R_{out}}{\partial k}\frac{\partial k}{\partial \rho_1} + \frac{\partial R_{out}}{\partial \rho_1}\right)^2 \Delta \rho_1^2 + \left(\frac{\partial R_{out}}{\partial k}\frac{\partial k}{\partial \rho_2} + \frac{\partial R_{out}}{\partial \rho_2}\right)^2 \Delta \rho_2^2}, \tag{2.96}$$

which can be explicitly estimated using eqs. (2.86,2.87,2.88,2.90,2.93,2.94).

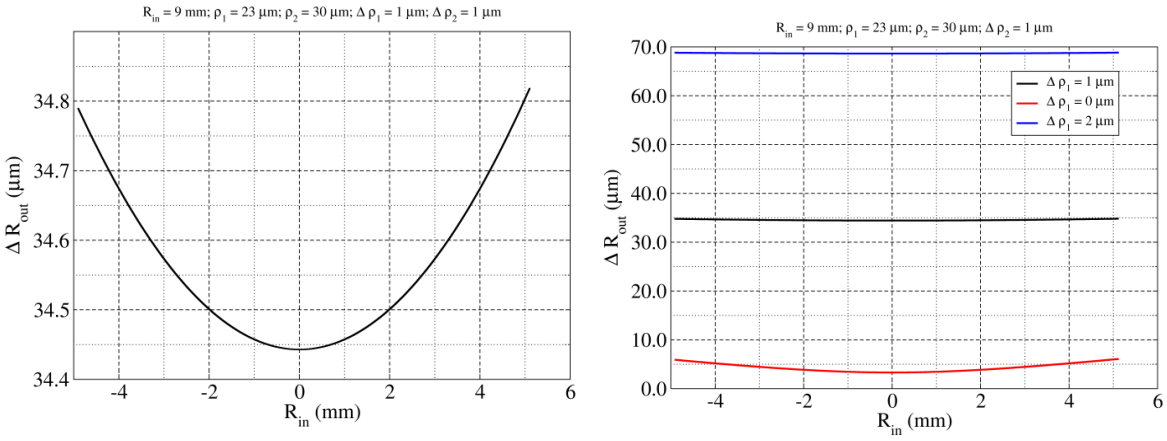

FIGURE 2.17. Left panel: Expected uncertainty on the output radius of curvature R_{out} as a function of the uncertainty on the input radius of curvature R_{in} for $\Delta\rho_1 = 1\mu m$. Right panel: same for three different values of $\Delta\rho_1$. The other parameters are marked on top of the graph. The left panel shows the detailed functional dependence as a function of ΔR_{in}, while the right one shows the evolution of the functions with $\Delta\rho_1$.

In the following figures, we illustrate the dependence of the expected uncertainty on the output radius of curvature R_{out} as a function of the uncertainties on the input radius of curvature R_{in}, of the radius of the first interference ring ρ_1, or of the second interference ring ρ_2. These graphs give an idea of the sensitivity of the estimate as a function of possible errors on each measurement.

It is important to remark that the expected value for $R_{out} = 283$ μm for the values of R_{in}, ρ_1 and ρ_2 chosen for the figure. This value is important to compare the size of the expected uncertainty to the actual radius of curvature. For graphical simplicity, the functional dependence of ΔR_{out} is plotted for one error at a time. The values of all parameters and other uncertainties are marked in the figure.

Fig. 2.17 shows the expected error in R_{out} as a function of a sizeable error (up to 5 mm) in the input radius of curvature. We see that the error on R_{out} is quite insensitive to the one on R_{in}, since it changes only by half a μm for ± 5 mm change in R_{in}. Therefore, we can conclude that a good determination of R_{out} does not depend on the quality of the estimate of R_{in}. In addition, the relative uncertainty is rather reasonable since it is approximately 12%. The near independence of ΔR_{out} signals is since the main contribution to the uncertainty comes from the other two variables. Indeed, suppose we attribute the

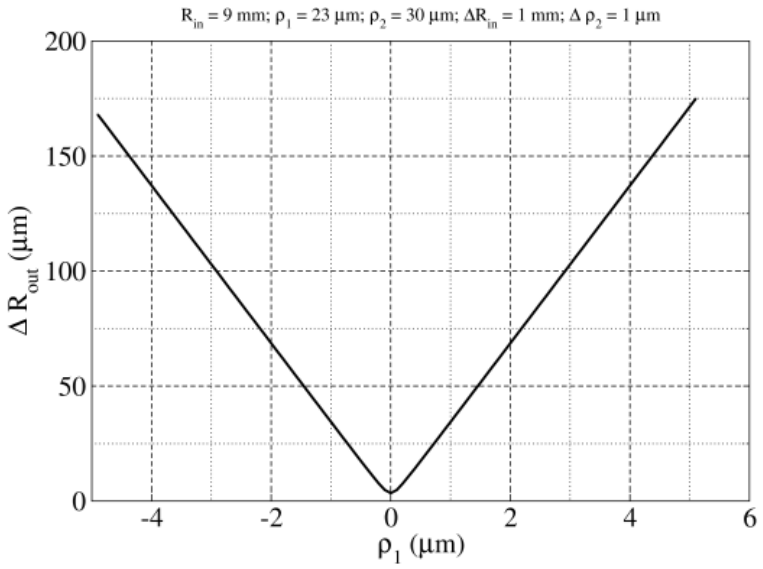

FIGURE 2.18. Expected uncertainty on the output radius of curvature R_{out} as a function of the uncertainty on the measurement of the radius of the first interference ring ρ_1. The other parameters are marked on top of the graph.

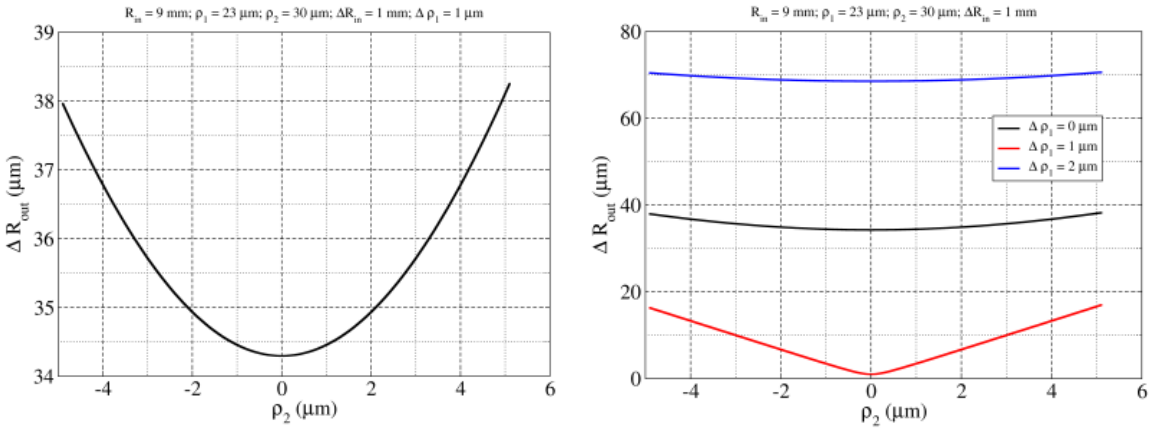

FIGURE 2.19. Left panel: Expected uncertainty on the output radius of curvature R_{out} as a function of the uncertainty on the measurement of the radius of the second interference ring ρ_2 for $\Delta\rho_1 = 1\,\mu$m. Right panel: same for three different values of $\Delta\rho_1$. The other parameters are marked on top of the graph. The left panel shows the detailed functional dependence as a function of $\Delta\rho_2$, while the right one shows the evolution of the functions with $\Delta\rho_1$.

variation of the uncertainty ($< 0.4\,\mu$m) to the influence of the error on R_{in}. In that case, we see that a relative error approximately equal to 11% (on R_{in}) produces a relative error contribution on R_{out} just above 0.1%. There is, therefore, a strong error suppression in this variable (nearly a factor of 100).

Fig. 2.18 shows the expected error in R_{out} as a function of the error on ρ_1, the radius of the first interference ring (interval $\pm 5\,\mu$m). Here there is a much stronger dependence on $\Delta\rho_1$, with a maximum uncertainty which takes a maximum relative value, in the plotted interval, approximately equal to 60% (for a maximum relative uncertainty on ρ_1 of 22%). This result shows a very high sensitivity on $\Delta\rho_1$, since the error is multiplied (nearly linearly, as shown in the graph) by a factor close to 3 – there is, therefore, a sensitive amplification of the error on $\Delta\rho_1$.

Finally, Fig. 2.19 shows the dependence of the expected error on R_{out} as a function of $\Delta\rho_2$, which, as $\Delta\rho_1$ has been taken to vary by $\pm 5\,\mu$m. The dependence is quite weak (nearly parabolic) with values which range from $34\,\mu$m to $38\,\mu$m, thus ensuring that the relative uncertainty coming from $\Delta\rho_2$ remains confined to at most 13% (for a relative uncertainty on ρ_2 up to 17%). In this case, there is an attenuation of the uncertainty propagated onto R_{out}. We thus conclude that only the uncertainty on ρ_1 has to be kept under control since it can introduce significant errors, which then propagate onto R_{out}.

2.4.2.2 Focal length

Using the results of the previous section for an estimate of the uncertainty on R_{out}, we now turn to computing the estimate for that on the focal length f_c. From previous calculations eq. (2.81), we find the focal length

$$
\begin{aligned}
f_c &= \frac{-d_1 \pm \sqrt{d_1^2 - 4d_2d_0}}{2d_2}, && (2.97)\\
d_2 &= (R_{in} - R_{out}) + (\tilde{L} + 2\mathscr{L}), && (2.98)\\
d_1 &= 2R_{in}R_{out} - (R_{in} - R_{out})(\tilde{L} + 2\mathscr{L}) - 2\mathscr{L}(\tilde{L} + \mathscr{L}), && (2.99)\\
d_0 &= -R_{in}R_{out}\tilde{L} + (R_{in} - R_{out} + \mathscr{L})\tilde{L}\mathscr{L}. && (2.100)
\end{aligned}
$$

In order to compute the uncertainty on f_c we need the following derivatives:

$$
\begin{aligned}
\frac{\partial f_c}{\partial d_2} &= \frac{d_1}{2d_2^2} \mp \frac{\sqrt{\Delta}}{2d_2^2} \mp \frac{1}{d_2}\frac{d_0}{\sqrt{\Delta}}, && (2.101)\\
\frac{\partial f_c}{\partial d_1} &= -\frac{1}{2d_2} \pm \frac{1}{2d_2}\frac{d_1}{\sqrt{\Delta}}, && (2.102)\\
\frac{\partial f_c}{\partial d_0} &= \mp\frac{1}{\sqrt{\Delta}}, && (2.103)
\end{aligned}
$$

where we have used the shorthand

$$
\sqrt{\Delta} = \sqrt{d_1^2 - 4d_2d_0}, \qquad (2.104)
$$

and the following explicit derivatives for the d_js as a function of the physical quantities $R_{in}, R_{out}, \tilde{L}$ and $\mathscr{L}$:

$$\frac{\partial d_2}{\partial R_{in}} = 1, \tag{2.105}$$
$$\frac{\partial d_2}{\partial R_{out}} = -1, \tag{2.106}$$
$$\frac{\partial d_2}{\partial \tilde{L}} = 1, \tag{2.107}$$
$$\frac{\partial d_2}{\partial \mathscr{L}} = 2, \tag{2.108}$$
$$\frac{\partial d_1}{\partial R_{in}} = 2R_{out} - (\tilde{L} + 2\mathscr{L}), \tag{2.109}$$
$$\frac{\partial d_1}{\partial R_{out}} = 2R_{in} + (\tilde{L} + 2\mathscr{L}), \tag{2.110}$$
$$\frac{\partial d_1}{\partial \tilde{L}} = -(R_{in} - R_{out}) - 2\mathscr{L}, \tag{2.111}$$
$$\frac{\partial d_1}{\partial \mathscr{L}} = -2(R_{in} - R_{out}) - 2(\tilde{L} + 2\mathscr{L}), \tag{2.112}$$
$$\frac{\partial d_0}{\partial R_{in}} = -R_{out}\tilde{L} + \tilde{L}\mathscr{L}, \tag{2.113}$$
$$\frac{\partial d_0}{\partial R_{out}} = -R_{in}\tilde{L} - \tilde{L}\mathscr{L}, \tag{2.114}$$
$$\frac{\partial d_0}{\partial \tilde{L}} = -R_{in}R_{out} + (R_{in} - R_{out} + \mathscr{L})\mathscr{L}, \tag{2.115}$$
$$\frac{\partial d_0}{\partial \mathscr{L}} = (R_{in} - R_{out} + 2\mathscr{L})\tilde{L}. \tag{2.116}$$

With these expressions, we can explicitly compute the uncertainty on f_c as a function of the uncertainties on R_{in}, R_{out}, $\tilde{L}$, and $\mathscr{L}$, by using the same chain rule:

$$\frac{\partial f_c}{\partial x_j} = \frac{\partial f_c}{\partial d_i}\frac{\partial d_i}{\partial x_j}, \tag{2.117}$$

where x_j represents any of the physical variables and d_k stands for any of the d coefficients ($i = 0 \ldots 2$). The uncertainty on f_c then becomes

$$\Delta f_c = \sqrt{\left(\frac{\partial f_c}{\partial R_{in}}\right)^2 \Delta R_{in}^2 + \left(\frac{\partial f_c}{\partial R_{out}}\right)^2 \Delta R_{out}^2 + \left(\frac{\partial f_c}{\partial \tilde{L}}\right)^2 \Delta \tilde{L}^2 + \left(\frac{\partial f_c}{\partial \mathscr{L}}\right)^2 \Delta \mathscr{L}^2}, \tag{2.118}$$

with

$$\frac{\partial f_c}{\partial R_{in}} = \frac{\partial f_c}{\partial d_2}\frac{\partial d_2}{\partial R_{in}} + \frac{\partial f_c}{\partial d_1}\frac{\partial d_1}{\partial R_{in}} + \frac{\partial f_c}{\partial d_0}\frac{\partial d_0}{\partial R_{in}}, \tag{2.119}$$
$$\frac{\partial f_c}{\partial R_{out}} = \frac{\partial f_c}{\partial d_2}\frac{\partial d_2}{\partial R_{out}} + \frac{\partial f_c}{\partial d_1}\frac{\partial d_1}{\partial R_{out}} + \frac{\partial f_c}{\partial d_0}\frac{\partial d_0}{\partial R_{out}}, \tag{2.120}$$
$$\frac{\partial f_c}{\partial \tilde{L}} = \frac{\partial f_c}{\partial d_2}\frac{\partial d_2}{\partial \tilde{L}} + \frac{\partial f_c}{\partial d_1}\frac{\partial d_1}{\partial \tilde{L}} + \frac{\partial f_c}{\partial d_0}\frac{\partial d_0}{\partial \tilde{L}}, \tag{2.121}$$
$$\frac{\partial f_c}{\partial \mathscr{L}} = \frac{\partial f_c}{\partial d_2}\frac{\partial d_2}{\partial \mathscr{L}} + \frac{\partial f_c}{\partial d_1}\frac{\partial d_1}{\partial \mathscr{L}} + \frac{\partial f_c}{\partial d_0}\frac{\partial d_0}{\partial \mathscr{L}}. \tag{2.122}$$

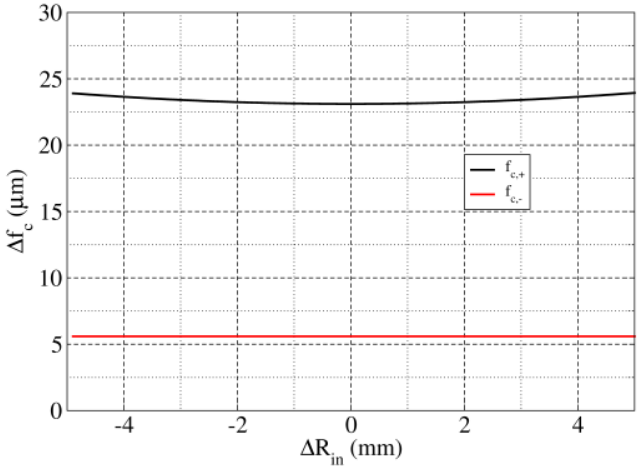

FIGURE 2.20. Expected uncertainty on the focal length determined from the experiment as a function of the uncertainty on the radius of curvature of the input beam. The two solutions are in black (positive sign in the quadratic formula) and red (negative sign). The resulting focal lengths are: $f_{c,+} = 350.63\,\mu$m, $f_{c,-} = 60.71\,\mu$m. Parameters: cell channel width $L = 180\,\mu$m, $n_w = 1.33$, coverslip thickness $t = 170\,\mu$m, $n_g = 1.5$, resulting in $\tilde{L} = 239.4\,\mu$m and $\mathscr{L} = 374.7\,\mu$m. The radius of curvature for the output beam is the one already obtained from $\rho_1 = 23\,\mu$m and $\rho_2 = 30\,\mu$m for $R_{in} = 9$ mm, i.e., $R_{out} = 282.63\,\mu$m. The uncertainties that have been ***fixed*** for this figure are the following: $\Delta R_{out} = 10\,\mu$m, $\Delta\tilde{L} = 10\mu$m, $\Delta\mathscr{L} = 10\,\mu$m.

Fig. 2.20 shows the evolution of the expected uncertainty over a broad interval of uncertainty values for the input radius of curvature. As already seen for R_{out}, the uncertainty is insensitive to ΔR_{in} and probably mostly due to the other uncertainties. Although small, it is not negligible. In particular, for $f_{c,-}$ it amounts to approximately 10%.

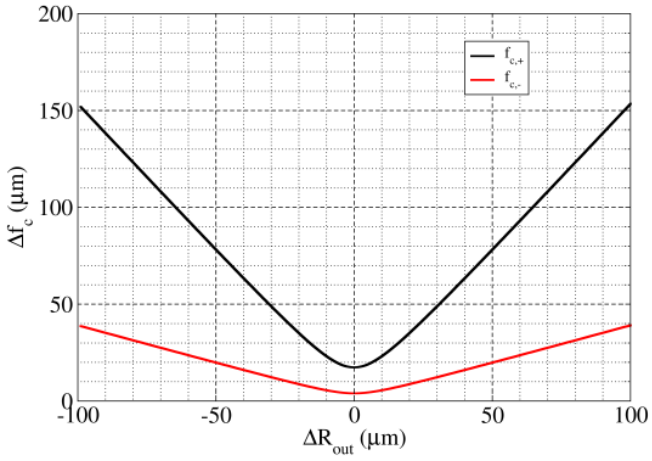

FIGURE 2.21. Expected uncertainty on the focal length determined from the experiment as a function of the uncertainty on the radius of curvature of the output beam. The two solutions are in black (positive sign in the quadratic formula) and red (negative sign). The uncertainty on the input beam radius of curvature is 1 mm. All other parameters and data as in Fig. 2.20.

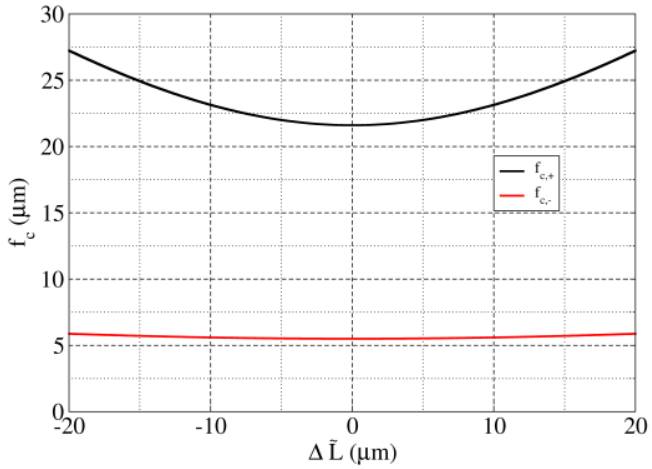

FIGURE 2.22. Expected uncertainty on the focal length determined from the experiment as a function of the uncertainty on the distance $\tilde{L}$. The two solutions are in black (positive sign in the quadratic formula) and red (negative sign). The uncertainty on the input beam radius of curvature is $1mm$. All other parameters and data as in Fig. 2.20.

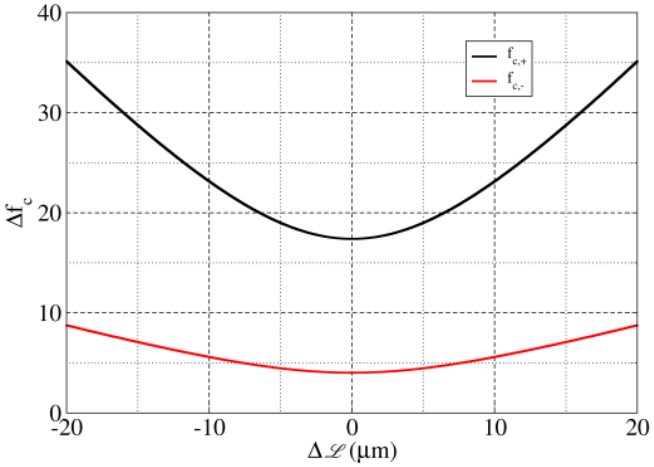

FIGURE 2.23. Expected uncertainty on the focal length determined from the experiment as a function of the uncertainty on the distance $\mathscr{L}$. The two solutions are in black (positive sign in the quadratic formula) and red (negative sign). The uncertainty on the input beam radius of curvature is $1mm$. All other parameters and data as in Fig. 2.20.

Fig. 2.21 shows again the strong sensitivity to the uncertainty in R_{out}, which dominates the others. In turn, its relatively high uncertainty is due to the strong influence of the uncertainty of ρ_1 in the determination of the output radius of curvature. The other two figures, Fig. 2.22 and Fig. 2.23, instead show a weak influence on the uncertainty of f_c.

2.5 Chapter summary

In section 2.1, a detailed description of the Acoustofluidic Interferometric Device (AID) and its principle of operation are presented. For clarity, this analyses the instrument as three separate subunits: 1) the experimental unit, which handles the cells and their deformation; 2) the detection unit, and 3) the control electronics. The experimental unit consists of a microfluidic chip equipped with a piezoelectric transducer that focusses all cells in the channel's center plane and deforms them when the acoustic wave has a sufficient intensity. Transverse to the chip a Fabry-Perot cavity is built, to perform precise (interferometric) measurements of the cell's optomechanical properties. The detection unit consists of an image acquisition device (CCD camera), for extracting information from the interferometric pattern. In parallel, two photodiodes whose scope is to acquire temporal cuts of the CFPP for real-time analysis. The electronics, based on Raspberry Pi modules interfaced to a master computer, control the AID's whole operation.

The main instrumental features can be summarized as follows: the device receives a steady flow of cells through a microfluidic system. Acoustic focussing is achieved through the piezo-generated acoustic wave, tuned to the microfluidic channel's (fundamental) resonance frequency $\nu_R = \frac{v}{2L}$ (cf. section 2.1). It is important to stress that accurate measurements of the optomechanical properties rely on the position control introduced by acoustic ocussing, enabling cell contactless and global deformation through the application of the force to the whole cell (sections 2.1 and 3.2).

Laser beams – used for the interferometric measurements in the AID – are well described by Gaussian beam theory, reviewed in section 2.2. Concepts as Rayleigh length and beam waist are introduced in relationship to beam propagation in the FP resonator, together with an explicit discussion of beam divergence and determination of beam spot size inside the cavity: the region in which the strongest (cf. section 3.1.2) is observed (cf. section 3.1.2).

Two different experimental configurations for cytometry can be distinguished on the basis of the ratio between the Fabry-Perot resonator length L and cell diameter ℓ (cf. section 2.3). The difference between the two configurations is not restricted to the pure requirements of the setup. Still, it is based on the interferometer's response, as in one case, one expects a shift in the fringe pattern, in the other one a fringe modification. If $L \approx 2\ell$ (cf. Fig. (2.11), matching a small-gap interferometer), the main effect of observing will be a shift in the Airy's transmission function. On the contrary, if $L \gg \ell$, the observed phenomenon will be a thin lens-like perturbation in the RFP. The low-Finesse configuration needed in the large-gap Fabry-Perot interferometer has been chosen due to its high throughput potential in optomechanical properties-based cytometry and its suitability to implement the acoustic manipulation of cells.

The CFPP can be modeled as thin lens perturbation (cf. section 2.4). The mathematical model used to describe the cell-resonator interaction is developed using ray-matrices. Using this parallel, it is possible to associate a focal length to a cell (CFL, cf. eq. (2.81)). The CFL, together with the Finesse (based on FWHM and FSR) are the parameters used to summarize and analyze the optomechanical properties of the cells. An uncertainty analysis is carried out (based on the CFL mathematical model) to identify the experimental parameters that should be carefully controlled while performing the experiments, where the error on ρ_1 ρ_1 – the distance between the resonator axis and the first fringe pattern– is the most sensitive parameter (cf. section 2.4.2). The uncertainty analysis is also helpful to discuss the AID optimization (cf. section 4.1).